Received: 12 January 2023 | Revised: 17 August 2023 | Accepted: 18 October 2023

DOI: 10.1002/qj.4607

Quarterly Journal of the Royal Meteorological Society RMetS

RESEARCH ARTICLE

Nowcasting convective activity for the Sahel: A simple probabilistic approach using real-time and historical satellite data on cloud-top temperature

Seonaid R. Anderson[1] | **Steven J. Cole**[1] | **Cornelia Klein**[1,2] | **Christopher M. Taylor**[1,3] | **Cheikh Abdoulahat Diop**[4] | **Mouhamadou Kamara**[4,5]

[1]UK Centre for Ecology & Hydrology, Wallingford, UK

[2]Department of Atmospheric and Cryospheric Sciences, University of Innsbruck, Innsbruck, Austria

[3]National Centre for Earth Observation, Wallingford, UK

[4]Agence Nationale de l'Aviation Civile et de la Météorologie, Dakar, Senegal

[5]GoldFarb School of Nursing, Barnes-Jewish College, St Louis, Missouri, USA

Correspondence
Seonaid R. Anderson, UK Centre for Ecology & Hydrology, Wallingford, UK.
Email: seodey@ceh.ac.uk

Funding information
Natural Environment Research Council (NERC), Grant/Award Numbers: NE/P021077/1, NE/S006087/2, NE/X006247/1

Abstract

Flash flooding from intense rainfall frequently results in major damage and loss of life across Africa. In the Sahel, automatic prediction and warning systems for these events, driven by Mesoscale Convective Systems (MCSs), are limited, and Numerical Weather Prediction (NWP) forecasts continue to have little skill. The ground observation network is also sparse, and very few operational meteorological radars exist to facilitate conventional nowcasting approaches. Focusing on the western Sahel, we present a novel approach for producing probabilistic nowcasts of convective activity out to six hours ahead, using the current location of observed convection. Convective parts of the MCS, associated with extreme and heavy precipitation, are identified from 16 years of Meteosat Second Generation thermal–infrared cloud-top temperature data, and an offline database of location-conditioned probabilities calculated. From this database, real-time nowcasts can be quickly produced with minimal calculation. The nowcasts give the probability of convection occurring within a square neighbourhood surrounding each grid point, accounting for the inherent unpredictability of convection at small scales. Compared to a climatological reference, formal verification approaches show the nowcasts to be skilful at predicting convective activity over the study region, for all times of day and out to the six-hour lead time considered. The nowcasts are also skilful at capturing extreme 24-hour rain gauge accumulations over Dakar, Senegal. The nowcast skill peaks in the afternoon, with a minimum in the evening. We find that the optimum neighbourhood size varies with lead time, from 10 km at the nowcast origin to around 100 km at a six-hour lead time. This simple and skilful nowcasting method could be highly valuable for operational warnings across West Africa and other regions with long-lived thunderstorms, and help to reduce the impacts from heavy rainfall and flooding.

KEYWORDS

convection, floods, forecasting (methods), local or boundary layer scale, observational data analysis, rainfall, severe weather

1 | INTRODUCTION

Flash flooding from heavy rainfall is a cause of major damage and loss of life in Africa (e.g., Engel *et al.*, 2017). Roca and Fiolleau (2020) show that across the tropics, long-lived mesoscale convective systems (MCSs) are closely associated with extreme precipitation events. Over the Sahel, these systems account for around 90% of the total seasonal rainfall (Mathon *et al.*, 2002; Nesbitt *et al.*, 2006), with convective rainfall accounting for around two thirds of the total rainfall for mature Sahelian MCSs. There is a pressing need to improve prediction of these events as the frequency and intensity of extreme rainfall over the Sahel is increasing (Panthou *et al.*, 2018) and contributing to an increase in the socio-economic impacts of African floods over recent decades (e.g., Di Baldassarre *et al.*, 2010; Tramblay *et al.*, 2020). Furthermore, the annual number of intense Sahelian MCSs has tripled since 1982 and this upward trend is expected to continue under climate change (Taylor *et al.*, 2017).

Over sub-Saharan Africa, Numerical Weather Prediction (NWP) forecasts have little skill (e.g., Vogel *et al.*, 2018), both due to the convective processes that operate (Keat *et al.*, 2019; Reinares Martínez & Chaboureau, 2018), and the difficulty in capturing the current meteorological state with a sparse observation network (Kniffka *et al.*, 2020). Currently, there are also very few operational radars over most of Africa, including West Africa (e.g., Roberts *et al.*, 2021), from which to estimate and predict precipitation. In contrast, geostationary satellite data provide a valuable source of high-frequency, high-resolution radiation observations of the earth and its atmosphere. Futyan and Del Genio (2007) explain that cloud-derived variables from these satellite observations do not provide a direct skilful proxy for convective rain. However, recent studies (Klein *et al.*, 2018; Klein & Taylor, 2020) have developed 2-D wavelet methods for identifying convective cores within MCSs from thermal–infrared imagery, highlighting cloud areas with strong association with heavy and extreme precipitation.

Very-short-range weather forecasting of the next few hours ahead based on recent observations, known as 'nowcasting' (e.g., Browning, 1982) is not currently widely used in Africa (Roberts *et al.*, 2021), but has huge potential to improve short-lead-time warnings of extreme high-impact precipitation. Given the lack of operationally available weather radars in the region, recent studies have focused on near real-time (NRT) nowcasting approaches based on geostationary satellites (Burton *et al.*, 2022; Roberts *et al.*, 2021). Hill *et al.* (2020) demonstrate useful forecast skill out to 90 minutes for extrapolated convective rainfall rate (CRR), and rapidly developing thunderstorm convection warning (RDT-CW) products, which give information on potential storm direction and current state of development based on atmospheric motion vectors and storm object tracking (cf. ZAMG, 2017). Both products are provided by the European Organisation for the Exploitation of Meteorological Satellites (EUMETSAT, 2022a, 2022b) Nowcasting Satellite Applications Facility (NWCSAF, 2022). Separately, Burton *et al.* (2022) apply a simple optical flow method based on pysteps (Pulkkinen *et al.*, 2019) to advect CRR images forward in time, and show that the extrapolated CRR has skill for 2 hours at 10-km scales and 4 hours at 200-km scales. All described methods use recent observations to deterministically extrapolate the future tracks of identified convection but do not allow for storm initiation, and decay. However, the longevity and strong diurnal cycle of MCSs in the Sahel (e.g., Maranan *et al.*, 2018), suggests potential for a probabilistic nowcasting approach based on climatological information from long satellite records that can complement existing object-based extrapolation methods.

Due to the unpredictability of small-scale convective processes and features ($\lesssim$10–30 km^2) (Hohenegger & Schär, 2007; Melhauser & Zhang, 2012; Prein *et al.*, 2021), a coarser spatial scale must be used to calculate useful and meaningful probabilistic forecasts of convective activity. Neighbourhood approaches (e.g., Schwartz & Sobash, 2017 and references therein) provide a method of generating probabilistic forecasts at scales larger than the grid scale of the NWP model for both deterministic and ensemble forecasts. The use of neighbourhood methods for forecast verification is also increasingly common (e.g., Ebert, 2008; Gilleland *et al.*, 2009), particularly for small-scale fields where traditional grid point verification results in the 'double penalty' problem — that is when forecasts with slightly different precipitation locations compared to observations are penalised twice: once for being a missed event, and again for being a false positive.

Here we present and assess a novel approach co-developed with West African forecasters under the Nowcasting FLood Impacts of Convective storms in the Sahel (NFLICS) project (UKRI, 2022). The approach uses the historical satellite record, constrained on the current location of observed convective structures (Klein *et al.*, 2018; Klein & Taylor, 2020), to produce skilful probabilistic nowcasts of convective activity out to six hours ahead. A neighbourhood method is used, based on maximum probabilities of a convective structure occurring within a particular area (e.g., Schwartz & Sobash, 2017) and appropriate spatial scales are identified for operational NRT use based on analysing probabilistic convective activity nowcast performance over a long period.

The underlying historical satellite data and precipitation data, used for method development and verification, are described in Section 2, along with a description of the

domains considered and the method for convective structure identification. Next, the procedure for generating NRT probabilistic convective activity nowcasts is given in Section 3. Section 4 then presents a verification of these nowcasts, in terms of both predicting convective activity, and predicting surface rain gauge observations. Further discussion of the nowcasting methods, possible real-time implementation, and potential developments is given in Section 5, with the key conclusions presented in Section 6.

2 | OBSERVATION DATA AND STUDY AREA

2.1 | Meteosat second generation thermal–infrared cloud-top temperature

We exploit the extensive Meteosat Second Generation (MSG) thermal–infrared cloud-top temperature (CTT) dataset, available at 15-min time intervals for the years 2004–2019 from the EUMETSAT Earth Observation Portal data archive (EUMETSAT, 2022b). Here IR 10.8 (channel 9) 'High Rate SEVIRI Level 1.5 Image Data – MSG – 0 degree' data were used. This is a widely used channel for identifying MCSs in Africa (Taylor *et al.*, 2017) and has long formed the basis of satellite rainfall estimation based in infrared imagery (e.g., Maidment *et al.*, 2014). Over the MSG period we have data for 97.6% of the possible times without systematic data gaps, having first filtered out images with obvious missing areas. Maidment *et al.* (2014) analysed the multidecadal Meteosat brightness temperature record and found no evidence of systematic temperature biases over the MSG period, so we have confidence in the use of this data.

The months June, July, August and September were selected covering the wet season in the Sahel, for a domain extending from around 20° W to 0° W and around 8° N to 20° N. This domain, shown in black in Figure 1 (left panel), was selected to capture the development of storms that reach Senegal, our country of focus. Over this domain, the MSG CTT data has a grid spacing of approximately 3 km. Three subdomains were considered for verification of the probabilistic nowcasts (Section 4.2) as shown in Figure 1: west of 12° W (W; red dotted), 12° W to 6° W (C; cyan dotted) and 6° W to 0° W (E; white dotted).

Within the extensive cloud envelope of MCSs, only certain regions are convectively active. It is these substructures that are linked to extreme rain, and the risk of sudden flash floods. Convective structures are identified from each MSG image (interpolated onto a 5-km grid) using a 2D-wavelet-transform method based on that presented in Klein *et al.* (2018) and summarised briefly here for ease of reference. First, areas of cold cloud (less than −40°C) are identified from the MSG image. A wavelet scale decomposition is then applied to the cold-cloud field for a range of scales (25–50 km) with a Marr wavelet transform. The wavelet power values are summed over the different scales considered, with convective structures identified where the summed power values exceed a scale-dependent threshold. In this work, the minimum power threshold is defined as $\Sigma(s+f)^{0.5}$, where s corresponds to the wavelet scale, and f represents an empirical variable that homogenises core detection frequencies across different datasets with $f=-8$ corresponding to the MSG period. Summing over the square root ensures a stronger weighting of small scales within the organised cold-cloud envelope, which are associated with higher probabilities for extreme rain than larger scales (Klein *et al.*, 2018). Finally,

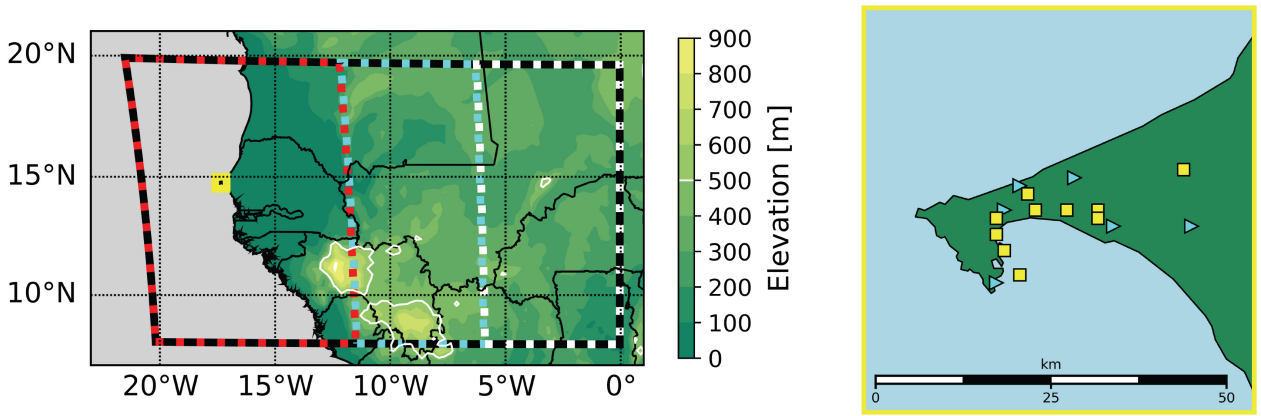

FIGURE 1 The West African domain used in this study is shown (left, black dotted polygon) along with the three subdomains used for verification: west of 12°W (W, red dotted), 12°W to 6°W (C, cyan dotted) and 6°W to 0°W (E, white dotted). Contours show the topography of the region, with the white 500-m contour highlighting the Guinea Highlands. Rain gauge locations over the Dakar region (left, yellow polygon) are also shown (right). Automatic rain gauge locations are shown by a cyan triangle, manual rain gauge locations by a yellow square. [Colour figure can be viewed at wileyonlinelibrary.com]

convective structures with power maxima co-located with cloud-top temperatures greater than −50°C are discarded. The wavelet scale decomposition is skilful in detecting cloud-top temperature gradients associated with convective cores within cold-cloud shields, but is also sensitive to gradients associated with cloud edges. Here, where we only consider cold-cloud <−40°C, power maxima associated with temperatures >−50°C are close to cloud edges (by definition) and are thus removed as likely artefacts. In addition, cloud-top temperatures >−50°C are unlikely to be associated with high-intensity rainfall in the considered region (Klein *et al.*, 2018). The locations of power maxima are retained as a single-point reference location for each convective structure.

2.2 | Rain gauge 24-hour accumulation data

In partnership with Agence Nationale de l'Aviation Civile et de la Météorologie, (ANACIM, the national meteorological agency of Senegal), 24-hour accumulation data for 16 rain gauges over the Dakar region covering the western peninsula of Senegal were available for independent nowcast verification. The rain gauge locations are shown in the right panel of Figure 1, covering the region highlighted in yellow in the left-hand panel. Six rain gauges are automatic (cyan triangle), with 24-hour recording periods from 0600 UTC, and data available post September 2017. Ten rain gauges are manual (yellow squares), with 24-hour recording periods from 0800 UTC, and data available in the period 2006–2013. The daily rain gauge values are summarised in Figure 2.

3 | METHODS

Our approach is to use a long-term conditional climatology to map the probability of convective structures out to six hours ahead given the location of currently observed convective activity. Firstly (Section 3.1.1), climatological probabilities of convective structures ($P(C)$) are calculated using data from all dates in the historical period H (June to September, 2004 to 2019). This definition of $P(C)$ gives the largest possible historical sample for the wet season in Senegal and represents a simple method from which future studies can build. Times of day are considered separately to preserve the diurnal cycle. Secondly (Section 3.1.2), we calculate climatological probabilities of convective structures out to six hours ahead using data from the historical period from a specific time of day but *conditioned on a convective structure being present with a power-maxima location* $\boldsymbol{x}_0$, $P(C_t|\boldsymbol{x}_0)$. Finally (Section 3.2), we present how the conditional climatological probabilities of convective structures out to six hours ahead (from Section 3.1.2) can be combined to form real-time nowcasts out to six hours based on multiple convective structures identified at the nowcast origin, $P(C_t|\boldsymbol{X}_0)$.

3.1 | Gridded convective structure probabilities derived from historical data

3.1.1 | Full climatological probabilities $P(C)$

The *full climatological probabilities of convective activity* $P(C)$ give a static overview of diurnal and spatial variations in convective probability, and provide a baseline for

FIGURE 2 Precipitation 24-hour accumulation values for the 16 Dakar rain gauges used for verification. Data from the 10 manual rain gauges are shown from 2006 to 2013, with data from the six automatic rain gauges shown from 2017. Each rain gauge is shown by a different colour–shape combination. [Colour figure can be viewed at wileyonlinelibrary.com]

assessing the effect of adding further conditions to the probability calculations. To calculate $P(C)$, convective activity was first defined as having occurred at any grid point in the domain (Figure 1) covered by any part of a convective structure (identified using the method presented in Section 2.1), creating binary grids C^b with values of one where convective structures were present or zero otherwise. Next the average was taken over C^b at each grid point, for each time of day, to give the fraction of dates in H with convective activity at each grid point, $P(C)$.

Although $P(C)$ can be calculated at the 5-km grid scale (as defined above), it is important to consider the utility of this information, given the exact location of convection is often uncertain and unpredictable at such high spatial granularity. Although large-scale precipitation and the overall characteristics may be predictable, the exact location and features of fine-scale embedded convective structures are less so. Spatially averaging or smoothing these grid point probabilities is one option, but this results in a reduction in their values. As the spatial averaging scale increases, this can result in probabilities that are of little meaning or value, and are not useful for warning purposes.

Therefore, instead of focusing on convection probability for a given location at the dataset resolution of 5 km, we use a neighbourhood maximum approach (Schwartz & Sobash, 2017) to consider the probability for convection occurring anywhere within a larger area surrounding that location. Thus, we evaluate the probability of convection occurring anywhere within a range of distances from each grid point by applying a spatial maximum filter of different filter lengths (Schwartz & Sobash, 2017) to C^b before calculating the probabilities for each grid point. Here a uniform square filter of length L (measured in multiples of the 5-km grid point resolution) is used, centred upon the grid point in question. For example, a filter of $L = 15$ km contains 3^2 grid points: the central point where the filter is being applied, and the eight grid points surrounding this central point. We define the *spatial scale* L of the probabilities to be equal to the filter size applied to the binary fields from which the probabilities are calculated. Defined in this way, L represents the minimum spatial distance over which differences between grid point values can be resolved.

An appropriate spatial scale must be chosen over which to calculate the probabilities, between the grid scale where spatial uncertainties dominate the results and probabilities are low but high spatial detail is preserved, and the domain scale where spatial uncertainties are highly reduced and probabilities increased, but all spatial detail is lost. Here, a range of spatial scales from $L = 15$ to 155 km were considered, and the appropriateness of each scale defined by the skill of the final nowcasts at that scale (Sections 4.2 and 4.3).

Figure 3 shows the full historical climatological probability of convective structures for $L = 45$, and 95 km

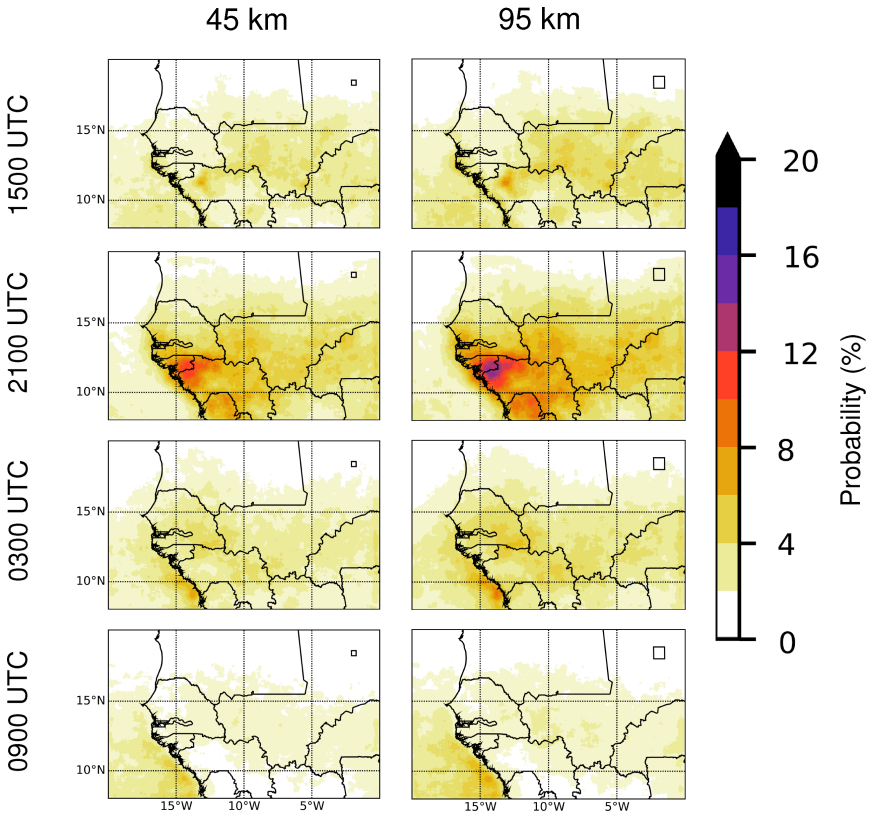

FIGURE 3 Full historical climatological probabilities of convective structures $P(C)$ during JJAS shown for four example times of day (rows; 1500, 2100, 0300, and 0900 UTC) and two example spatial scales (columns; 45 km and 95 km, shown by the solid black square). [Colour figure can be viewed at wileyonlinelibrary.com]

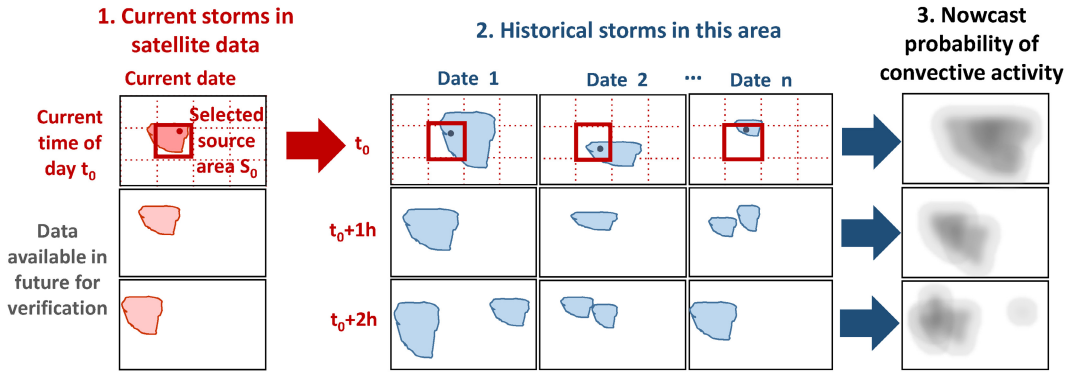

FIGURE 4 Schematic showing the method of calculating climatological probabilities conditional on convective structure location $P(C_t|\boldsymbol{x}_0)$: (1) Current storm in satellite data at time of day t_0 (red), the power maxima location, $\boldsymbol{x}_0$ (red dot) and selected source area, S_0 (solid red box); (2) historical storms (blue) from the associated historical dates H_0 that have their power maxima location (blue dot) in the same source area at time of day t_0; and (3) nowcast probability of convective activity, $P(C_t|\boldsymbol{x}_0)$ (greyscale, darker shades indicate higher probabilities). [Colour figure can be viewed at wileyonlinelibrary.com]

(columns), and four times of day (rows): afternoon (1500 UTC) when convection tends to initiate, evening (2100 UTC) where convective activity is often well developed, overnight (0300 UTC) when convection is mostly decaying, and in the morning (0900 UTC) where there is little convective activity over land. As expected from the 'maximum' method of calculating neighbourhood probabilities, the probability values increase with L. In this work, a range of L are considered to determine the minimum neighbourhood size needed to give useful and meaningful probability grids, while maintaining the maximum possible spatial detail (Sections 4.2 and 4.3). Overall, we can see the effect of elevated terrain causing higher probabilities over the Guinea Highlands (around 15°W, 12°N, see Figure 1). The morning peak in convection over the ocean can also be seen. A clear north–south variation in convective activity occurs, with the highest probabilities seen around 12°N. The wet season (JJAS) climatological probabilities for the focus region of Dakar, and for most of Senegal, are very low, below 10% even for the largest spatial scale ($L = 95$ km) considered and during the evening peak of storm activity (see 2100 UTC).

3.1.2 | Climatological probabilities conditional on convective structure location $P(C_t|\boldsymbol{x}_0)$

In order to obtain probabilities for nowcasting, the current convective state can give additional information alongside that obtained from the full climatology $P(C)$. Here we investigate the utility of using climatological probabilities of convective structures over the next six hours conditioned on the (power maxima) location $\boldsymbol{x}_0$ of a current convective structure, $P(C|\boldsymbol{x}_0)$. For convection at $\boldsymbol{x}_0$, falling within a particular source area S_0, we calculate $P(C|\boldsymbol{x}_0)$ as follows. First, we consider the set of historical dates H_0 (a subset of the full historical period H), where convection occurred at this time and in this source area (S_0). Averaging over these grids gives $P(C_0|\boldsymbol{x}_0)$, the conditional probability of convection occurring, at each grid point in the domain, at time t_0 ('now'). Averaging over H_0 at later times of day gives $P(C_i|\boldsymbol{x}_0)$, the conditional probability of convection occurring, at each grid point in the domain, at these times. For clarity of expression, we have abbreviated the lead time dependence notation, thus: $C_i = C(t_i)$. The steps in calculating $P(C_i|\boldsymbol{x}_0)$ are shown schematically in Figure 4 for a theoretical nowcasting example where an $\boldsymbol{x}_0$ has been selected based on a real-time MSG CTT image. In the study region where diurnal variability in convection is high (e.g., Futyan & Del Genio, 2007), these conditional climatological probabilities, $P(C_t|\boldsymbol{x}_0)$, implicitly provide predictability over the next few hours. For example, a convective core identified in the morning hours is far more likely to decay in the next three hours than one in mid-afternoon. Similarly, the strong meridional gradient in convection which characterises the Sahel favours longer-lived convection in the south compared to the north.

Given an MSG CTT image, the locations of convective structures were identified using the methods of Section 2.1, and each location was associated with a particular S_0. The neighbourhood approach described in Section 3.1.1 was then applied to create C^{b} at different spatial scales L for each identified historical date, both at t_0 and for the following six hours (t_1, t_2, …, t_6). For a given source area S_0, taking the average at each grid point over the subset of grids that had a convective location $\boldsymbol{x}_0$ within S_0 at t_0, gives the conditional probability grids appropriate for the current time and the next six hours: $P(C_0|\boldsymbol{x}_0)$, $P(C_1|\boldsymbol{x}_0)$, … $P(C_6|\boldsymbol{x}_0)$.

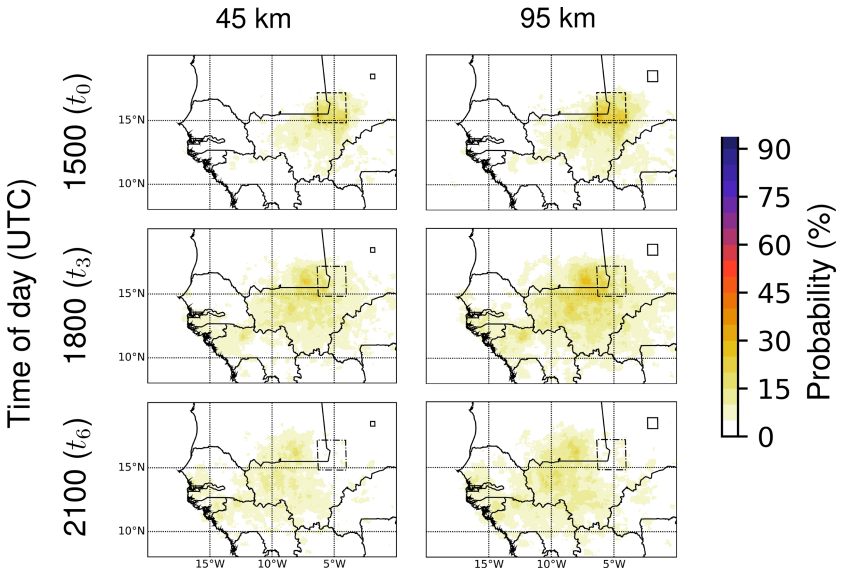

FIGURE 5 $P(C_t|\boldsymbol{x}_0)$ for an example S_0 at $t_0 = 1500$ UTC (top), t_3 (1800 UTC, middle) and t_6 (2100 UTC, bottom) for example spatial scales $L = 45$ km and 95 km (shown by the solid black square in the top right of maps). S_0 is shown by the black dashed square (t_0) and dash–dotted squares (t_3 and t_6). [Colour figure can be viewed at wileyonlinelibrary.com]

An important consideration is how to select the size and location of the source areas S_0 such that they are sufficiently large to each select a *meaningful sample* of historical dates H_0, yet sufficiently small to be useful in a forecasting context and to select only points originating from a single, distinct MCS. These considerations vary with location, time of day, and the specifics of H_0, so no single precise S_0 setup covers all of them. Here all available MSG CTT data from 2004 to 2018 were used to calculate the minimum S_0 size needed to obtain a specified number of historical dates N for each grid point in the domain, and for each hour in the day. Values of N between 40 and 100 were analysed as this was found to be a sufficient sample to give spatially consistent probability values at a useful granularity. From a visual analysis of all of these results (not shown), and considering the historical distribution and size of convective storms in the Sahel (Guy & Rutledge, 2012; Klein *et al.*, 2018; Maranan *et al.*, 2018), an appropriate source area was found to be 81×81 native MSG grid points (at this latitude around 250×250 km; 62,500 km^2). Further refinements to vary S_0 by time of day and geographic location were considered, but it was decided that this level of complexity was not warranted at this initial stage in the system development.

Figure 5 shows probabilities for lead times of zero, three, and six hours ($P(C_0|\boldsymbol{x}_0)$, $P(C_3|\boldsymbol{x}_0)$ and $P(C_6|\boldsymbol{x}_0)$) from a t_0 of 1500 UTC, for $\boldsymbol{x}_0$ falling within an example source area S_0, and using spatial scales $L = 45$ and 95 km. The highest probabilities are seen within S_0, as every grid contributing to probability has, by definition, a convective structure within S_0. As the example L lengths are smaller than the S_0 length (250 km), these highest probabilities never reach 100%. Similar to the results of $P(C)$ (Figure 3), higher probabilities are seen at larger scales due to the maximum neighbourhood method applied. In this example, the peak probabilities decrease with lead time for all L due to the dispersion of convective structures away from S_0, and the diurnal cycle of convective activity. This trend is seen in general for other S_0, and times of day. However, there are instances where the probabilities increase with increasing lead time, for example where climatologically convective structures are strengthening and initiating. Figure 5 also highlights how higher probabilities are not constrained to S_0: although convective structures occurred by definition within S_0, there is no constraint on them also occurring (or not) at other points in the domain. The maps of $P(C_t|\boldsymbol{x}_0)$ reflect the climatological progression and initiation/decay of convection in the region, implicitly including fixed topographic effects and the general east–west propagation. For example, consider the Guinea Highlands (around 13° W, 12° N). As discussed above (Figure 3), the orography in this region leads to high levels of convection in the late afternoon, reflected here in increased probabilities of convection around 1800 UTC in $P(C_3|\boldsymbol{x}_0)$. As lead time increases, we see the peak probability values translating westwards, the dominant direction of storm propagation.

To enable $P(C_t|\boldsymbol{x}_0)$ to be efficiently pre-calculated for many different $\boldsymbol{x}_0$, a set of overlapping source areas S_0 was created. The central part S'_0 of each S_0 is unique, constructed of 41×41 native MSG-grid grid points. Each S_0 overlaps with those adjacent to it by 20 grid points, ensuring that consistent conditional probabilities are obtained for adjacent S_0. An example S_0 is shown by the red square 'A' in Figure 6. As the predominant movement of convective storms in the Sahel is westward, S_0 are not considered over the Atlantic, however, to ensure that all costal land-areas are covered, S_0 are stretched south and west

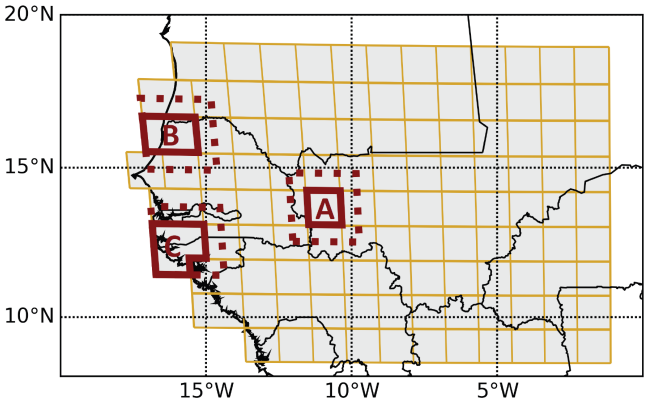

FIGURE 6 Map showing the locations of the 112 unique S'_0 (41 × 41 native, ~3 × 3 km Meteosat Second Generation [MSG] grid point). The full S_0 extends for a further 20 grid points north, south, east and west of the block-coloured square. The full (red dashed) and central (red solid) parts of S_0 are highlighted for three example S_0. Example A shows the setup for inland S_0. In coastal examples B and C, S'_0 are stretched south and west to ensure that all costal land-areas are covered. [Colour figure can be viewed at wileyonlinelibrary.com]

along the coast (e.g., 'B' and 'C' in Figure 6). Note that although a given convective structure location, $\boldsymbol{x}_0$, will fall within multiple S_0 areas, it will only fall within one S'_0 which is then used to calculate $P(C_t|\boldsymbol{x}_0)$.

3.2 | Real-time nowcast conditional on convective structure locations $P(C_t|\boldsymbol{X}_0)$

To create a real-time convective activity nowcast, a set of S_0 are selected from the most recent real-time MSG CTT image. First, the convective structures and their locations ($\boldsymbol{X}_0 = \{\boldsymbol{x}_0{}^1, \boldsymbol{x}_0{}^2, \ldots \boldsymbol{x}_0{}^n\}$) at t_0 are identified using the method presented in Section 2.1. Each convective feature location $\boldsymbol{x}_0{}^1, \boldsymbol{x}_0{}^2, \ldots \boldsymbol{x}_0{}^n$ is then associated with a particular S_0, using the unique central S'_0 grid. Figure 7 shows an example for the 26 August 2012 at 0000 UTC with convective structures identified from the MSG CTT grid (top left) and the associated set of S_0 (top centre).

Once the set of S_0 appropriate to the real-time satellite image have been identified, the associated probability grids for each individual S_0 are combined to give *one conditional probability grid* for each lead time appropriate to all the locations of convection identified within the real-time image. The maximum probability is taken at each grid point of the conditional probability grids obtained for the set of individual S_0 selected, such that the real-time convective activity nowcast is given by $P(C_t|\boldsymbol{X}_0) = \mathrm{MAX}[P(C_t|\boldsymbol{x}_0{}^1), P(C_t|\boldsymbol{x}_0{}^2), \ldots, P(C_t|\boldsymbol{x}_0{}^n)]$. The maximum is preferred over other simple combination strategies, because it ensures that each individual grid point is only taking the probability from one S_0. This is necessary because one particular historical date can be included in the set of associated historical dates H_0 for multiple S_0. Data from each lead time are separately combined. Although this approach will not be optimal for all cases, it provides a simple basis from which more complex combination methods can be developed.

The right-hand column of Figure 7 shows probabilistic nowcast grids $P(C_t|\boldsymbol{X}_0)$ for an example spatial scale of $L = 95$ km (19 × 19 grid points from the 5-km constant-resolution grid used for convective structure identification). To aid comparison, the convective structures identified from the MSG CTT at the evaluation time for each forecast lead time are also shown (left column). Note that, apart from at the nowcast origin time t_0 (here 0000 UTC 26 August 2012) these observations would be unavailable in a real-time forecasting context. At time t_0, the set of eight source area locations selected for this nowcast (Figure 7, top middle) from the origin time MSG CTT grid (Figure 7, top left) are clearly seen as square regions of high probability in the t_0 nowcast grid (Figure 7, top right). This is because, by definition, all the H_0 for a given S_0 will have at least one convective structure within the source area at this time. Higher probabilities are seen towards the centre of each S_0, as the convective structures (irrespective of L) are more likely to overlap (giving higher probabilities) closer to the centre of the constraining area S_0 (e.g., Dey *et al.*, 2016). As the nowcast lead time increases, the nowcast probabilities decrease due to the convective regions from the historical grids dispersing spatially away from the selected S_0, losing coherence, and convection initiating and decaying.

4 | VERIFICATION

Three types of verification were used to understand and objectively evaluate the nowcast performance. First, C^{b} extracted at Dakar rain gauge locations were verified directly against the rain gauge data (Section 2.2) to assess the ability of the convection detection method to capture observed precipitation values (Section 4.1). Next, the probabilistic convective activity nowcasts, $P(C_t|\boldsymbol{X}_0)$ (Section 3.2), were verified against the observed convective structures, C^{b}, corresponding to the *evaluation times* of the forecasts (Section 4.2). This provides an indication as to the success of the forecasting methodology for obtaining forward predictions, and can be applied at all locations in the domain, for all historical years, with no further data requirements. Verification is performed for different L using the neighbourhood method described in Section 3.1 which is applied to both the forecasts and the observations C^{b}. Finally, $P(C_t|\boldsymbol{X}_0)$ were verified against 24-hour precipitation rain gauge accumulations from the Dakar region of Senegal (Section 4.3). Although for a limited

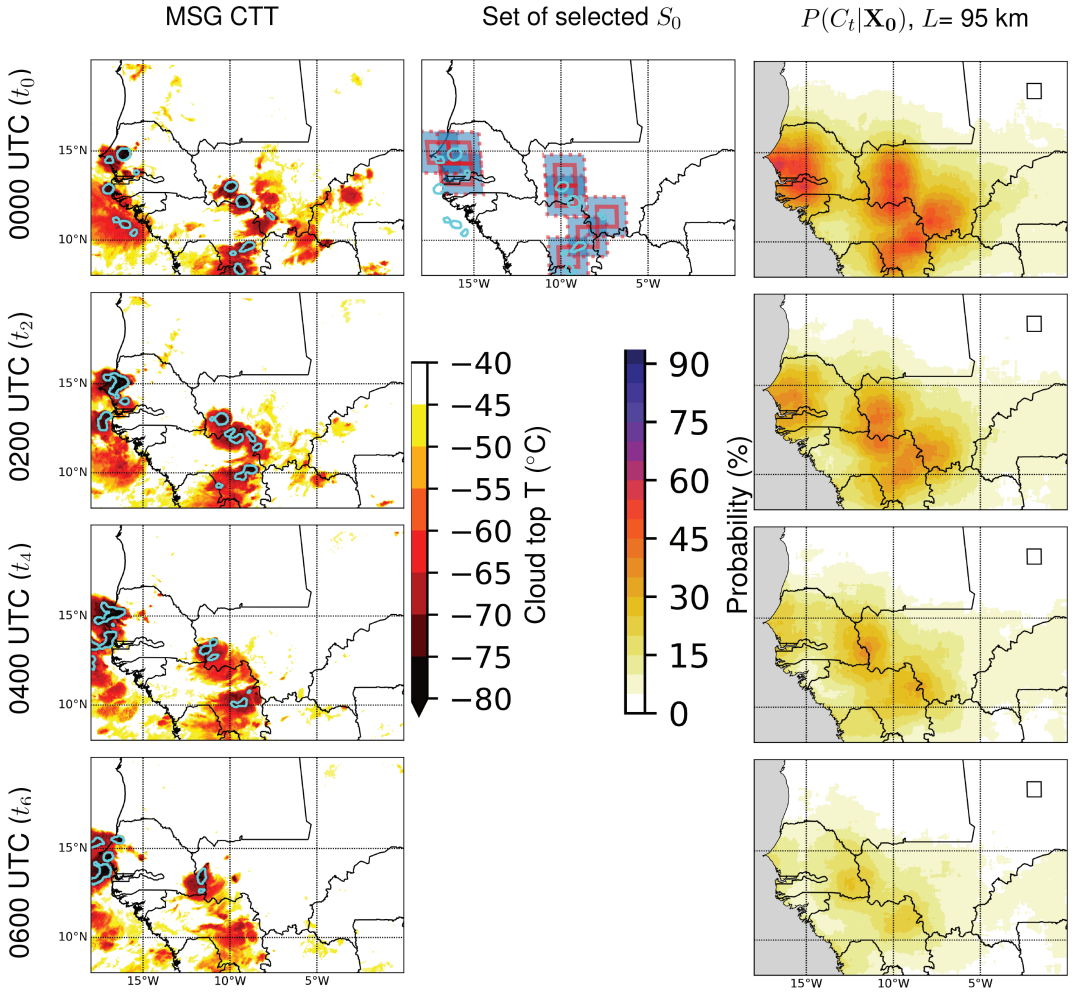

FIGURE 7 Example convective structures (left) for 0000, 0200, 0400 and 0600 UTC on the 26 August 2012. The Meteosat Second Generation cloud-top temperature (MSG CTT, °C) is shown (filled contours), along with the identified convective structures (cyan contours). For a nowcast origin of 0000 UTC, the set of S_0 selected are shown by pale blue squares with dotted red outlines (middle) for the convective structures identified at this time (top-left). The central unique part of each S_0 is shown by a solid red outline. The probabilistic nowcast grids $P(C_t|\boldsymbol{X}_0)$ are also shown (right), for an example L of 95 km (shown by the black square), at nowcast origin t_0 (0000 UTC) and lead times two hours (t_2, 0200 UTC), four hours (t_4, 0400 UTC) and six hours (t_6, 0600 UTC). [Colour figure can be viewed at wileyonlinelibrary.com]

geographical area, this verification against actual observed precipitation values is crucial to assess the performance of the probabilistic nowcasts for forecasting *heavy* and *extreme precipitation* events.

Although the verification method applied here to *probabilistic* nowcast grids is similar to the verification method commonly applied to *ensemble* forecast probabilities, an important difference is that here, there is no ensemble. Hence it is not possible to calculate statistics based on ensemble average measures (such as the root mean square error, or ensemble mean), or based on individual member behaviour (such as the continuous ranked probability skill score or rank histogram). Here we assess $P(C_t|\boldsymbol{X}_0)$ using the reliability diagram, sharpness diagram, and Brier skill score (BSS) (e.g., Wilks, 2011). The reliability diagram plots probability of the observation given the forecast (the *observed relative frequency*) against the forecast probability. This allows the *reliability*, a measure of whether the forecast probabilities are a true representation of reality, and *resolution*, an indication of how much the forecast deviates from the reference, to be visually assessed. Perfect reliability is seen along the diagonal of the reliability diagram, whereas a forecast with no resolution (where the observed relative frequency equals the sample climatology) appears as a horizontal line. A sharpness histogram shows the sample size (*forecast relative frequency*) for each *forecast* probability bin. The BSS assesses the skill of probabilistic forecasts, measuring the proportional improvement in mean square probability error as defined by the Brier score, BS (Brier, 1950) with respect to a reference forecast $\mathrm{BS}_{\mathrm{ref}}$;

$$\mathrm{BSS} = 1 - \frac{\mathrm{BS}}{\mathrm{BS}_{\mathrm{ref}}}. \quad (1)$$

At best, BSS takes a value of one and values less than zero indicate the forecast performs worse than the reference.

To assess the bias-corrected potential of $P(C_t|\boldsymbol{X}_0)$, and its ability to capture and predict convective events given a particular probability threshold, we use the contingency table, counting the number of hits, misses, false alarms and correct rejections. This information is summarised by the hit rate, the fraction of hits to total events observed and the false alarm rate, the ratio of false alarms to total instances when no event is observed. The relative operating characteristic (ROC) diagram (e.g., Jolliffe and Stephenson, 2012) plots paired values of hit rate and false alarm rate for a given probability threshold to assess the potential skill of probability forecasts, that is, the skill if probabilities were well calibrated. The larger the area underneath each ROC curve (AUC), the better the forecast skill in identifying events while minimising false alarms. The ROC skill score (ROCSS) used here is constructed by comparing the area AUC to that produced from a reference forecast.

$$\mathrm{ROCSS} = 1 - \frac{\mathrm{AUC}_{\mathrm{ref}}}{\mathrm{AUC}}. \tag{2}$$

A ROCSS above zero indicates the forecast has a skill better than the reference forecast.

For the calculation of the BSS and ROCSS, we use the full climatological probabilities $P(C)$ from Section 3.1 as a reference. Thus, BSS and ROCSS values between above 0 show that the nowcasts $P(C_t|\boldsymbol{X}_0)$ are skilful, that is, outperforming the reference $P(C)$, with larger values corresponding to higher skill. Negative values show that the reference outperforms the nowcast; the nowcast is not skilful. For the ROCSS, using $P(C)$ as a reference leads to results indistinguishable from those compared to a random forecast (an $\mathrm{AUC}_{\mathrm{ref}}$ of 0.5), meaning a perfect forecast (an AUC of 1) would have a ROCSS value of 0.5.

4.1 | Verification of convective structure identification method for predicting extreme precipitation

The overall method for convective structure identification for extreme satellite-derived rainfall rates over the Sahel has been previously investigated using instantaneous rainfall rates from spaceborne radar (Klein *et al.*, 2018). However, this probabilistic relationship was established using data across the Sahel and relying on spaceborne radar only, which may exhibit systematic errors. A verification with rain gauges represents a reverse analysis to directly test the skill of our nowcast system to capture high-intensity rain based on independent in-situ data in the study region. Additionally, by verifying against 24-hour rain gauge data over the Dakar region of Senegal (Figure 1, right) we can evaluate the method's predictive ability for instances where rainfall totals are known to cause impact on the ground. All available rain gauge data are considered, with a rainfall threshold used to define binary time series of rainfall events equal to one if the threshold is exceeded, zero otherwise. Three thresholds are selected based on local forecasting experience. These correspond broadly to heavy (30 mm), flood producing (60 mm) and extreme (90 mm) 24-hour precipitation totals over the Dakar region. To ensure that the convective structure and observed precipitation data are as similar as possible, grid-scale convective structure data are extracted at the rain gauge locations: C^{b} (rain gauge). We consider a convective structure to 'cover' a rain gauge if any part of the convective structure covers the rain gauge grid point. Secondly, as C^{b} are calculated every 15-minutes, it is necessary to combine multiple C^{b} grids corresponding to the 24-hour rain gauge accumulation period. Here we consider a threshold on the number of times in the 24-hour period where C^{b} (rain gauge) is required to equal one to count as a convective event. Thresholds from 1 to 13 are considered, that is, requiring the convective structure and rain gauge i.e. to be coincident for between 15 and 180 minutes in a given 24 hour period. Note that these times do not need to be consecutive as we want to capture the total daily amount of precipitation due to convective activity.

The contingency table is used to compare the binary time series of C^{b} (rain gauge) (the 'forecasts') with the binary time series of rainfall events (the 'observations'). The four constituents of the contingency table – hit, miss, false alarm, and correct rejection – are plotted in the top row of Figure 8. These plots show the total number of events falling into each contingency table quadrant including data from all available rain gauge locations and times. As expected for the high rainfall thresholds selected, the number of observed events is much smaller than the number of instances where no event occurs, with the discrepancy increasing with the precipitation threshold used. As the C^{b} 24-hour threshold increases, the number of hits decrease and the number of misses increase. This suggests that the heavy precipitation events are frequently dominated by rapidly passing convective structures that are only present over a small number of 15-min time slices at the subdaily scale. This is consistent with the propagating nature of Sahelian MCSs, which cause transient precipitation bursts during the passage of their convectively active region.

To analyse further the performance of the convective structure identification method, the second row of Figure 8 shows the hit rate and the false alarm rate. Overall, both the hit and false alarm rates decrease as the C^{b} time threshold increases. Thus, by requiring convective structures for a greater fraction of the rain gauge accumulation period, the chances of missing an event are increased, whilst the

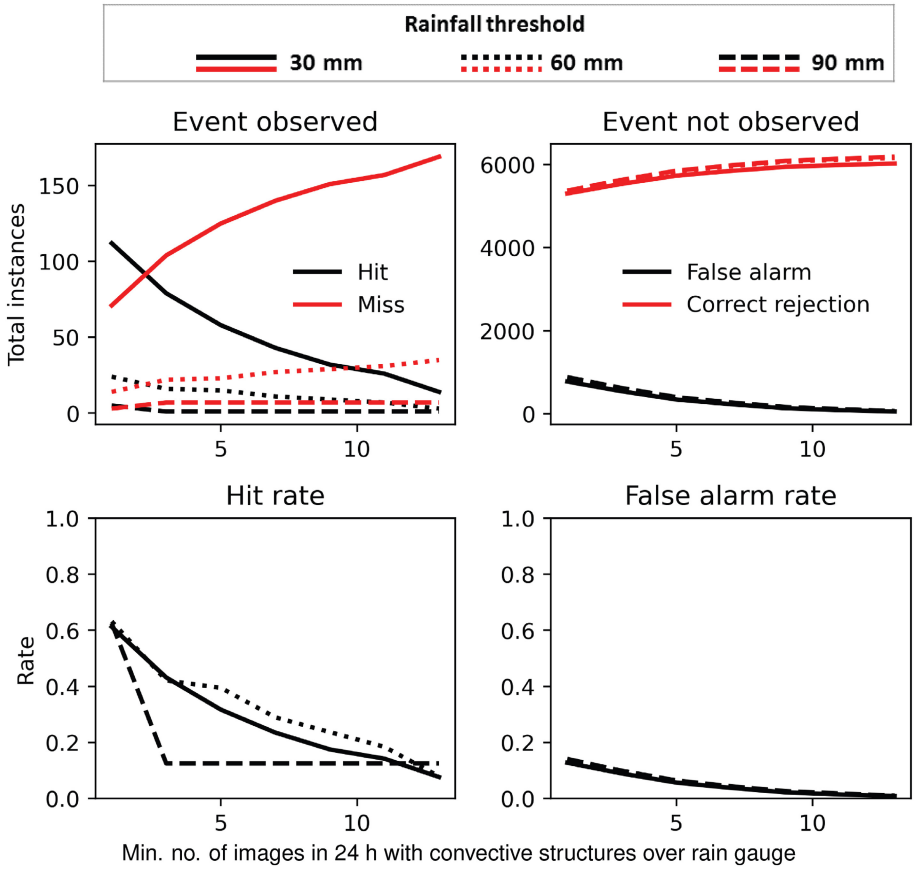

FIGURE 8 Contingency table constituents for the verification of C^b against 24-hour rainfall accumulations over Dakar for instances where an observed event occurs (Hit and Miss, top left) and does not occur (False alarm, Correct rejection, top right). Combined-measures Hit rate (bottom left) and False alarm rate (bottom right) are also shown. Results are shown for three precipitation thresholds (30 mm solid, 60 mm dotted, 90 mm dashed) as a function of the 24-hour C^b threshold, that is, the minimum number of images with convective structures covering each rain gauge in 24 hours needed to count as a forecast event (x-axis, identical for all subplots). [Colour figure can be viewed at wileyonlinelibrary.com]

chance of a false alarm occurring are reduced. The hit rate peaks around 0.6 for all rainfall thresholds, with a rainfall event associated with an identified convective structure 60% of the time. Given the large number of instances where no event is observed, the false alarm rates are much lower, peaking around 0.125. These results provide an important context in which to interpret the convective structure nowcasts in the context of extreme rainfall events. This will be discussed further in Section 5.

4.2 | Verification of forecasting method for obtaining forward predictions

In this section, the nowcast probability grids $P(C_t|\boldsymbol{X}_0)$ (the 'forecasts') are verified against the binary convective structure grids C^b at forecast evaluation time t (the 'observations'). Nowcasts were initiated hourly from June to September, for the 3 years from 2020 to 2022 with nowcast grids created hourly out to six hours (t_6). Each nowcast was created using the full climatological data from 2004 to 2019.

Nowcasts from four time-of-day ranges were verified separately: afternoon (1200–1700 UTC), evening (1800–2300 UTC), night (0000–0500 UTC) and morning (0600–1100 UTC), covering the main phases of the Sahelian diurnal cycle. Nowcasts were grouped by *nowcast origin time* t_0. Another possible grouping by forecast *evaluation time* leads to similar conclusions (Supplementary Figures S5 and S6 correspond to article Figures 9 and 10). To maintain spatial information on nowcast performance, and based on the propagation of storms in the Sahel from east to west, three longitude verification domains were used: West of 12°W (W), 12°W to 6°W (C), and East of 6°W (E), as shown in Figure 1. Data from all 4 months in the wet season (1 June – 30 September) are considered together, along with all land-based 5 km grid points in the longitude strip, and all times within the selected time window. For example, if a domain consisted of 10 grid points, there would be around 1 million forecast-observation pairs contributing to the verification calculations in the verification period (10 grid points × 122 days × 14 years × 6 hr). Nowcasts were evaluated at spatial scales L ranging from 5 km (the grid scale over which convective features are identified) to 155 km (35 grid points).

We first consider the forecast reliability, that is, the ability of the forecasts to capture the probability of occurrence of an event. Figure 9 shows reliability diagrams and sharpness histograms for two times of day, 1200–1700 UTC (top) and 0000–0500 UTC (bottom) for the W domain. As there are no higher-probability forecasts, the reliability lines are only shown at low probability bins containing at least 100 samples of data. Results are shown for $L = 45$ km (9 grid points; left) and 95 km (19 grid points; right). Focusing first on the top-left plot (1200–1700 UTC, $L = 45$ km),

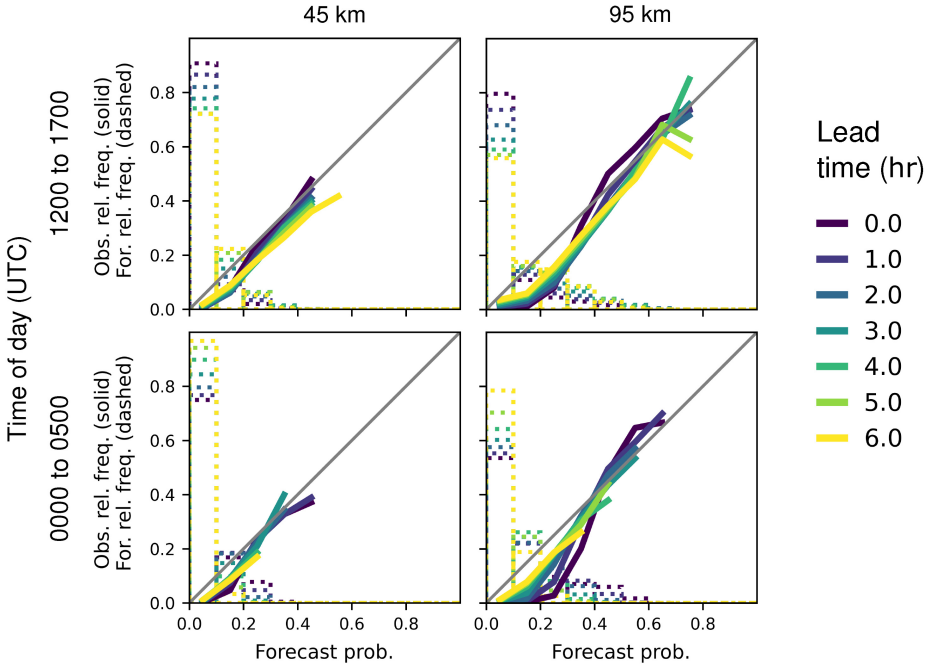

FIGURE 9 Reliability diagrams (solid) and sharpness histograms (dashed) for the verification of $P(C_t|\boldsymbol{X}_0)$ against $C^{\mathrm{b}}{}_t$ for the domain W. Colours show forecast lead time: yellow/light, lead time t_0 to purple/dark, t_6. Results are shown for two times-of-day windows, 1200–1700 UTC (top) and 0000–0500 UTC (bottom) and for two spatial scales, $L = 45$ km (left) and 95 km (right). Reliability diagrams are only plotted for sharpness histogram bins containing greater than 100 data points. [Colour figure can be viewed at wileyonlinelibrary.com]

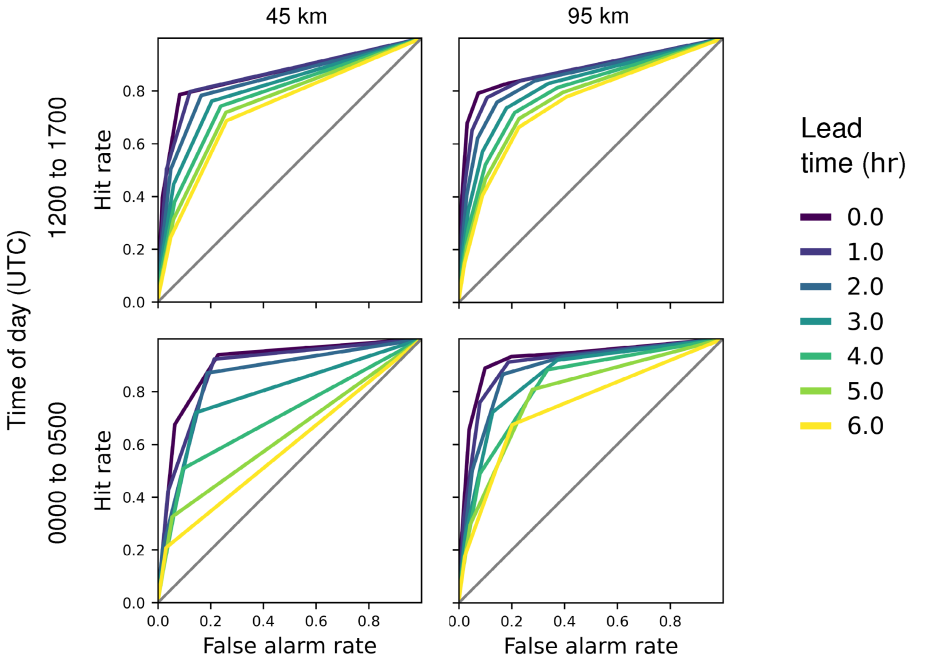

FIGURE 10 Relative operating characteristic (ROC) diagrams for the verification of $P(C_t|\boldsymbol{X}_0)$ against $C^{\mathrm{b}}{}_{\mathrm{t}}$ for domain W. Colours show forecast lead time: yellow/light, lead time t_0 to purple/dark, t_6. Results are shown for two time-of-day windows, 1200 to 1700 UTC (top) and 0000 to 0500 UTC (bottom) and for two spatial scales, $L = 45$ km (left) and 95 km (right). [Colour figure can be viewed at wileyonlinelibrary.com]

we see that the solid lines for all lead times fall below, but close and parallel to, the diagonal. Thus, the observed relative frequency is slightly lower than the forecast probabilities for a given probability bin: the forecast probabilities tend to be slightly too high for all probabilities considered. Similar results are seen for small L at other times of day (e.g., 0000–0500 UTC, bottom left). Although similar performance is seen across lead times, there is a tendency for the shorter lead times to have forecasts that are more reliable during the night and early morning. Considering the sharpness histograms for this L, we see that >95% of forecasts fall into the first two probability bins (0 to 0.2), with the remaining forecasts in bins 3 and 4 (0.2–0.4).

Overall, the reliability for forecast probabilities less than 0.4 is similar as L increases. For higher forecast probabilities, increasing L improves the reliability. The details of the scale-dependence depend on the forecast lead time and time-of-day window considered. As L increases, the forecast probability values also increase, with higher bins being populated in the sharpness diagrams, for example, by $L = 95$ km (right column) over 5% of forecasts have probabilities >0.5. In a way, by considering larger spatial scales we are artificially inflating the probability values. Comparison with rain gauge observations (Section 4.3) is needed to inform as to whether or not this is justified. For the largest L shown here ($L = 95$ km; right), the

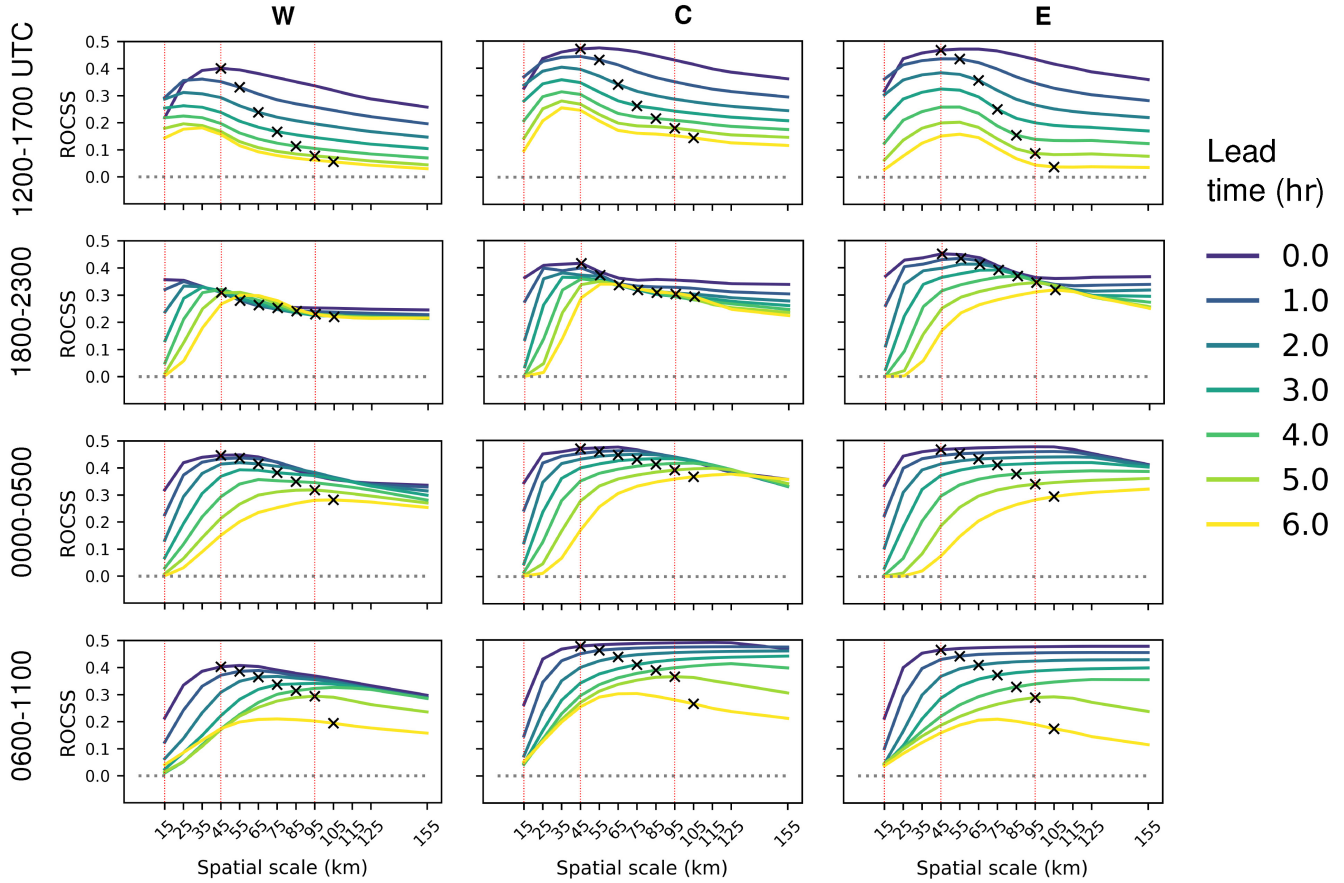

FIGURE 11 Relative operating characteristic skill score (ROCSS) of $P(C_t|\boldsymbol{X}_0)$ compared to $P(C)$ as a function of L. Colours show forecast lead time: yellow/light, lead time t_0 to purple/dark, t_6 for the four time-of-day windows split by forecast origin time (rows) and three verification domains considered (columns). Black crosses show ROCSS values for the L selected to use at each lead time (see text). Red dotted vertical lines mark the example L used in Figures 4, 5 and 7–10 (45 and 95 km), and the minimum L considered (15 km). [Colour figure can be viewed at wileyonlinelibrary.com]

performance in the first few hours of the forecasts is poorer than that at longer lead times for low probabilities, but is improved for high probabilities. The large L, and associated spatial smoothing of the probabilities (low probabilities increased, high probabilities reduced) results in underconfident predictions at short lead times. Thus the optimal L is time-varying throughout the nowcast, with smaller L more appropriate at shorter lead times. Similar results are found for the other verification domains (Supplementary Figures S1 and S3); the results for the three domains will be examined below in the comparison of skill scores (Figures 11 and 12 below).

We next examine how $P(C_t|\boldsymbol{X}_0)$ compares to C^{b} in an event-based framework, that is how, for a particular probability threshold, $P(C_t|\boldsymbol{X}_0)$ captures C^{b} in terms of hits, misses, false alarms and correct rejections. Figure 10 shows ROC diagrams for two times of day, 1200–1700 UTC (top) and 0000–0500 UTC (bottom) and spatial scales $L = 45$ km (left) and 95 km (right). All the nowcasts show some skill in this framework, with the ROC curves lying above the diagonal (ROC curve for a random forecast) for all lead times and times of day considered. Poorer skill is seen when levels of convective activity are low and decreasing (e.g., from 0000 to 0900 UTC). In Figure 10 this is seen in greater lead time variation in skill from 0000 to 0500 UTC, with poorer skill seen at longer lead times (i.e. predicting further into the morning). For all times of day the ROC diagrams show a clear increase in forecast skill with increasing L, and decrease in forecast skill for increasing nowcast lead time. These trends are much clearer than those seen for the reliability diagrams (Figure 9): the ROC diagrams are not sensitive to the bias in the probability forecasts affecting the reliability. As with the reliability diagrams, similar conclusions can be drawn from the ROC diagrams for the other verification domains (Supplementary Figures S2 and S4).

To assess the nowcast skill at capturing individual events, Figure 11 shows the ROCSS as a function of L for the four time-of-day windows considered (rows) and the three verification domains (columns). Each plot shows scores for each forecast lead time as a function of L. The example L used in Figures 4, 5 and 7–10 (45 and 95 km), along with the minimum L considered (15 km) are highlighted by the red vertical lines. For all the domains

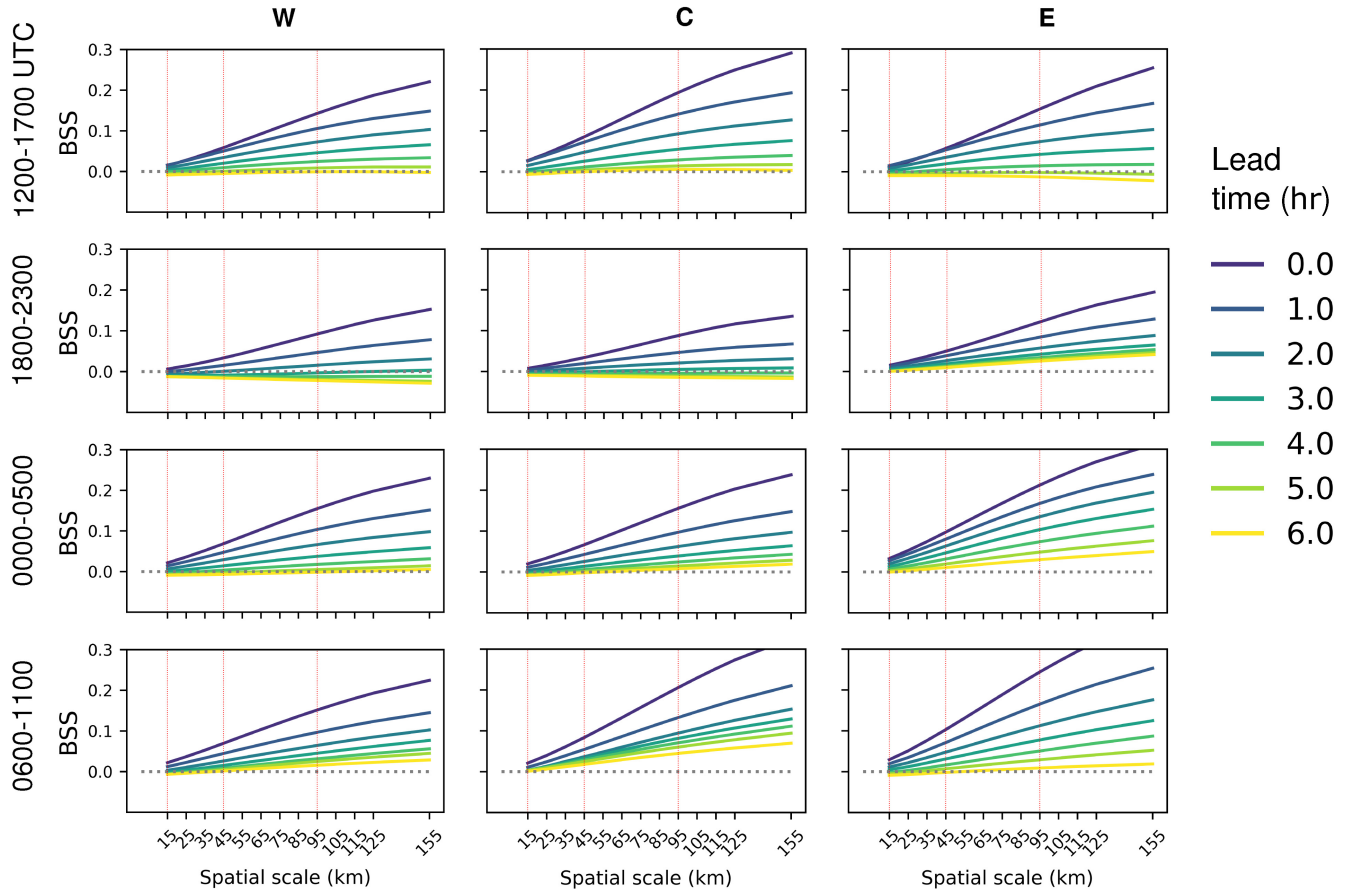

FIGURE 12 Brier skill score (BSS) of $P(C_t|\boldsymbol{X}_0)$ compared to $P(C)$ as a function of L. Colours show forecast lead time: yellow/light, lead time t_0 to purple/dark, t_6 for the four time-of-day windows split by forecast origin time (rows) and three verification domains considered (columns). Red dotted vertical lines mark the example L used in Figures 4, 5 and 7–10 (45 and 95 km), and the minimum L considered (15 km). [Colour figure can be viewed at wileyonlinelibrary.com]

and lead times considered, the ROCSS are positive and $P(C_t|\boldsymbol{X}_0)$ are skilful compared to $P(C)$. Overall, consistent with the ROC and reliability diagrams in Figure 9 and Figure 10, higher skill is seen for shorter lead time forecasts. After an initial strong increase in ROCSS with increasing L, further increases are less marked, with forecast origins from 1200 to 1700 UTC (all verification domains) and 1800 to 2300 UTC (domains W and C) showing a slight decrease in skill for the higher L considered. Overly smoothing out the probability fields has a detrimental effect on the prediction of convective events for these times and domains. Two additional verification domains, North (N) and South (S), combining longitudinal coverage of the W and C domains, were considered to further investigate the spatial dependence in afternoon and evening nowcast skill. This analysis (Supplementary Figures S7 and S8) found nowcasts for the N domain to be more skilful than those for the S domain, reflecting the occurrence of longer-lived and more-predictable convective structures further north. The ROCSS peaked at smaller L for the S domain, similar to the behaviour seen for the W and C domains, suggesting that the topographic influence on the convection from the Guinea Highlands may be constraining the spatial uncertainty in convection location.

For all times of day and domains, there is also a lead time dependence, with the ROCSS peaking at larger L for longer lead times, for example, for the E domain evaluated in the afternoon (top right plot) or W and C domains in the evening (second row, left and centre). In a well -performing ensemble system, the range of possibilities (spread) is representative of the true uncertainty in the forecast (skill) (e.g., Buizza, 1997; Leutbecher & Palmer, 2008). Statistically we would expect both the spread and uncertainty to increase with forecast lead time. Associated with this increase in uncertainty is an increase in the spatial scales needed to give a skilful ensemble forecast (e.g., Dey *et al.*, 2014). Here the differences between historical convective structures contributing to $P(C_t|\boldsymbol{X}_0)$ (the 'spread') increases with lead time (due to dispersion away from S_0) and the scale L needed to give peak skill increases.

TABLE 1 Spatial scales L values appropriate for each forecast lead time.

Lead time (hr)	0	1	2	3	4	5	6
L (km)	45	55	65	75	85	95	105
L (no. 5-km grid points)	9	11	13	15	17	19	21

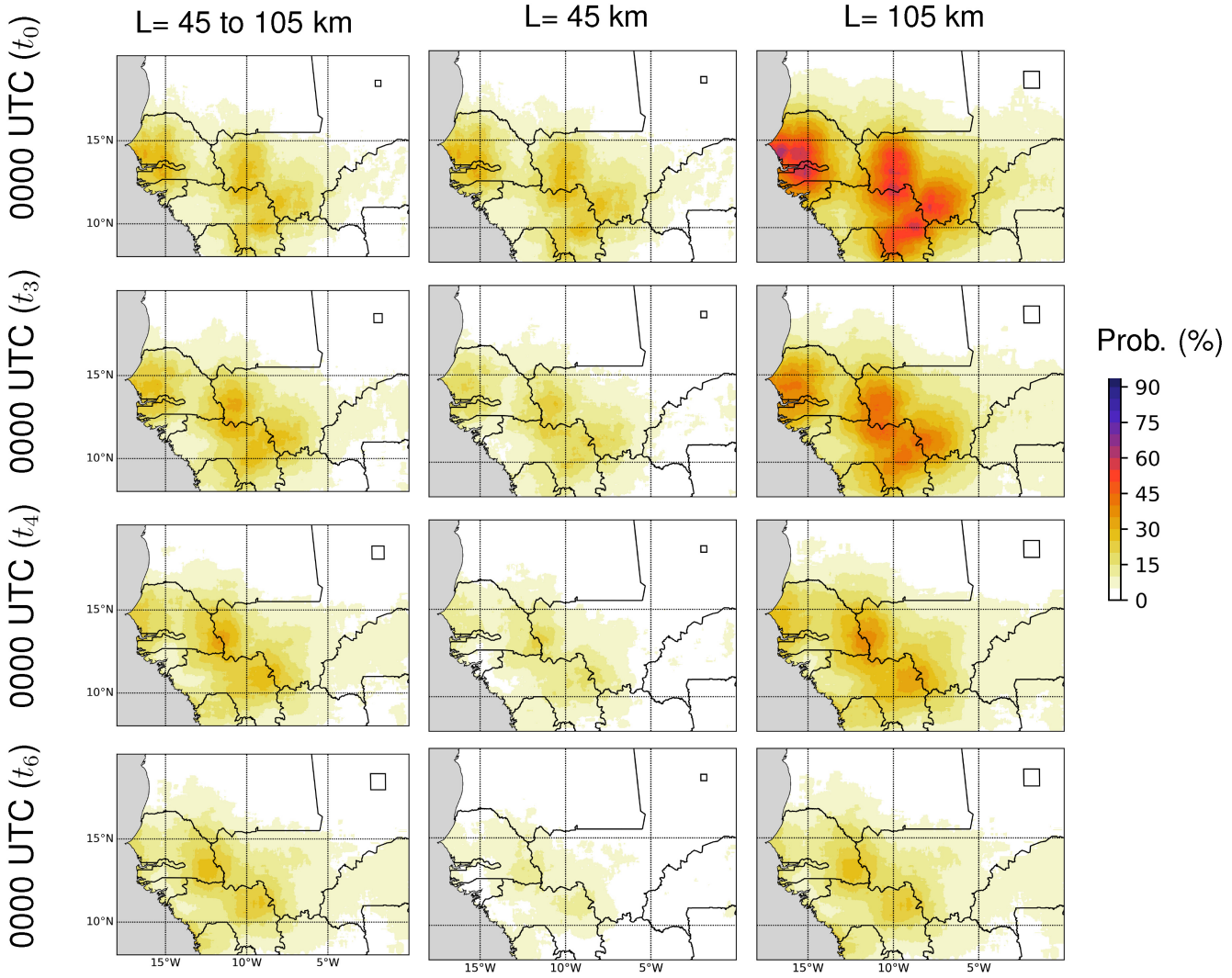

FIGURE 13 Example nowcast for 26 August 2012 0000 UTC. $P(C_t|\boldsymbol{X}_0)$ are shown for lead times of zero (t_0) to six hours (t_6) using L appropriate to each forecast lead time as given in Table 1 (left), for $L = 45$ (centre), and for $L = 105$ km (right). Each L is shown by the black square to the northeast of the domain. [Colour figure can be viewed at wileyonlinelibrary.com]

For operational use in NRT, it is desirable to select one L for use in each nowcast image, reducing the computation and simplifying visualisation and interpretation. Subjective analysis of Figure 11, along with the corresponding figures for forecasts grouped by forecast evaluation time (Supplementary Figure S5), and for the different verification periods considered, suggests that a workable approximation for obtaining the maximum skill is to have a spatial scale that increases with lead time. This relationship is approximately linear, ranging from spatial scales of 45 km at t_0 to 105 km for a t_6. The ROCSS at these scales are shown by the black crosses in Figure 11. Although more complex relationships could be developed, it is not believed that this additional complexity is warranted for this simple nowcasting system. Table 1 summarises the L values selected for each forecast lead time.

Figure 12 is identical in structure to Figure 11, but showing the BSS. Overall $P(C_t|\boldsymbol{X}_0)$ are skilful (positive BSS) compared to $P(C)$: conditioning the nowcasts based on the location of current convection leads to useful gains

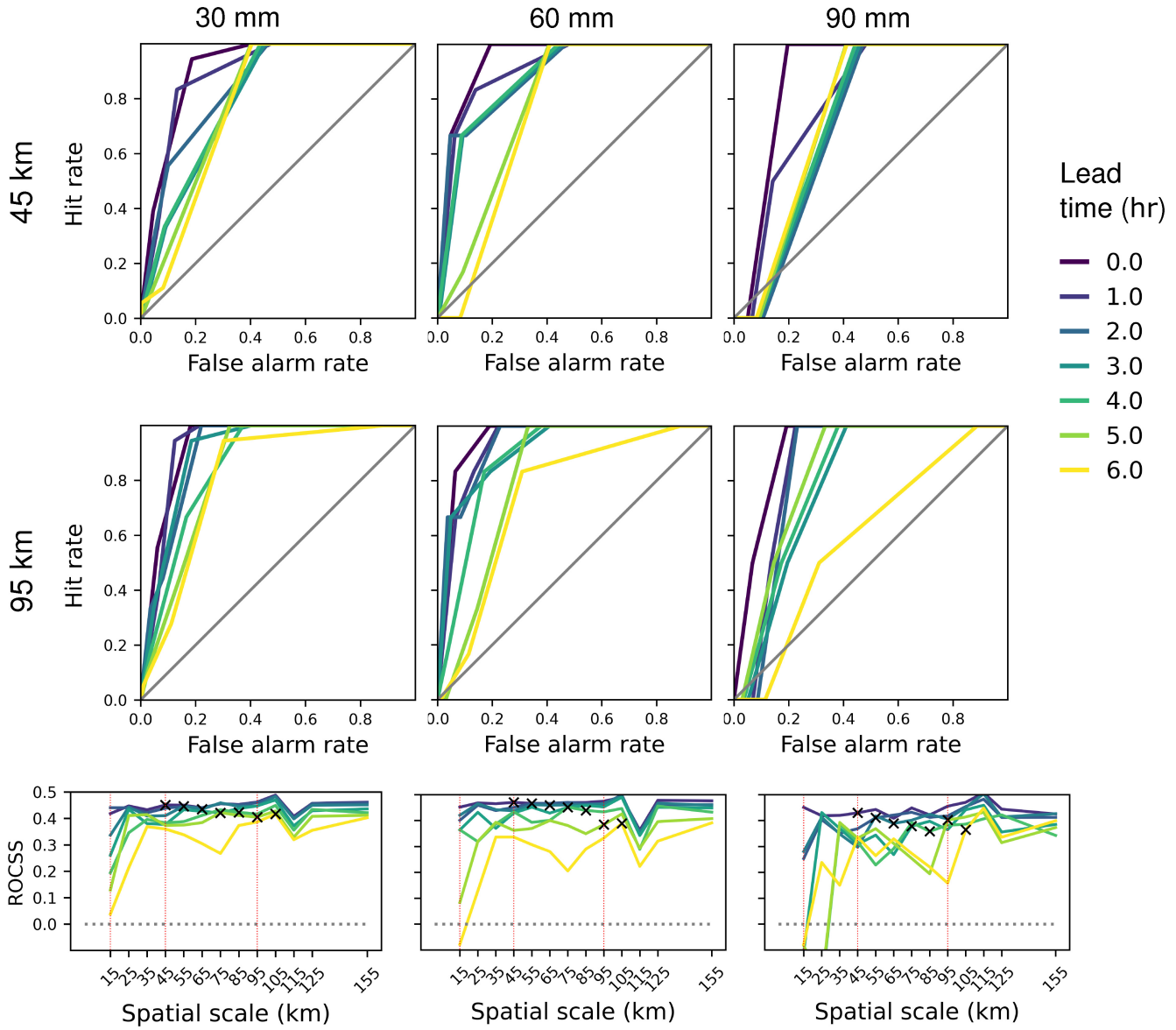

FIGURE 14 Relative operating characteristic (ROC) diagrams (top two rows) and ROC skill score (ROCSS) as a function of L (bottom) for the verification of $P(C_t|\boldsymbol{X}_0)$ against 24-hour rain gauge accumulations. Colours show forecast lead time: yellow/light, lead time t_0 to purple/dark, t_6 for rainfall thresholds 30 mm (left), 60 mm (centre) and 90 mm (right). Black crosses show ROCSS values for the L selected for real-time use. [Colour figure can be viewed at wileyonlinelibrary.com]

in skill for the probability values. The BSS shows skill increasing uniformly as L increases, at least for the range of scales considered here. Thus, the selection of the L values for each forecast lead time based on the ROCSS alone (Table 1) is appropriate.

Figure 13 shows the same nowcast example as shown in Figure 7 but using the L appropriate to each forecast lead time (left), and L of 45 km (centre, used for t_0) and L of 105 km (right, used for t_6). As L increases with lead time the effect on $P(C_t|\boldsymbol{X}_0)$ is consistent and smoothly varying across lead times. Overall, we see that varying L results in probability values that show less decrease with lead time. In particular, the larger L used at longer lead times increase the nowcast probability values as the spatial constraint on the precise location of convection is relaxed.

Further nowcasts can be viewed through the UKCEH Hydrology in Sub-Saharan Africa portal (UKCEH, 2023) which has been running nowcasts in real-time over JJAS since September 2021.

4.3 | Verification of forecast method for predicting rainfall events

The results of Section 4.2 provide a useful evaluation of the performance of $P(C_t|\boldsymbol{X}_0)$ for predicting convective activity. It is also necessary to evaluate the performance

of $P(C_t|\boldsymbol{X}_0)$ directly against observed rainfall. Here we verify against the 24-hour rain gauge accumulation data from Dakar, as used in Section 4.1 to assess the performance of C^{b}. For a meaningful comparison, all $P(C_t|\boldsymbol{X}_0)$ grids corresponding to each 24-hour rain gauge accumulation period are considered. It is possible for the occurrence of convection at any hour of the day to dominate the 24-hour precipitation total. Hence, to facilitate the comparison of a daily precipitation totals with hourly convective structures, the maximum probability is taken across all $P(C_t|\boldsymbol{X}_0)$ grids with evaluation times falling within the 24-hour rain gauge accumulation period. Each grid point and forecast lead time were considered separately. This comparison, although not exactly like-for-like, provides an indication as to the utility of $P(C_t|\boldsymbol{X}_0)$ for predicting extreme precipitation events. As it is more likely that any differences between these two measures will result in poorer verification results, the verification seeks to answer the question 'is this forecasting system viable' rather than 'how good is the forecasting system'. Here we focus on the ROC diagram and ROCSS as these are not sensitive to any probability bias incurred through the '24-hour maximum' treatment of $P(C_t|\boldsymbol{X}_0)$. Each rain gauge is compared to $P(C_t|\boldsymbol{X}_0)$ for the closest grid square to that rain gauge, for a range of L.

Figure 14 shows example ROC diagrams, for $L = 45$ km and 95 km (top two rows) for rainfall thresholds 30, 60, and 90 mm (columns). For all thresholds, ROC curves at small L (e.g., 45 km, top row) show poorer performance than those for larger scales. This is particularly seen at lead times greater than three hours where the $L = 45$ km curves lie very close to the 'random forecast' diagonal. For larger scales, the ROC scores are of comparable magnitude to those seen for the verification of $P(C_t|\boldsymbol{X}_0)$ against C^{b} (Figure 10). Overall, the ROC curves are similar for the three precipitation thresholds considered, with the exception of lead times t_5 and t_6 for the 90-mm threshold where poorer performance is seen, possibly due to the smaller sample size (e.g., Figure 2). The bottom row of Figure 14 shows the ROCSS as a function of L, with the example L values corresponding to the ROC diagrams above marked with red lines. Although these results are noisier than those for the verification against C^{b} (Figure 11), particularly for the 90-mm threshold where sampling uncertainties start to dominate, the pattern is the same, with higher skill seen for shorter lead times and larger L. Thus, the appropriate values of L to maximise the nowcast skill at each lead time, given in Table 1, are also an appropriate choice for increasing the skill of prediction for extreme precipitation events. Overall, considering both the ROC and ROCSS diagrams shows that $P(C_t|\boldsymbol{X}_0)$ is skilful at predicting convection leading to heavy, flood producing and extreme 24-hour precipitation accumulations over Dakar.

5 | SUMMARY AND DISCUSSION

This paper has presented and assessed a novel approach to produce probabilistic nowcasts of convective activity out to six hours ahead using historical satellite records, conditioned on the current location of observed convection. These nowcasts were shown to be skilful (compared to a full climatological reference) at predicting convective activity over a Western Sahelian domain, and for 24-hour precipitation accumulations over Dakar. When considering the skill in a contingency framework given by ROCSS, the nowcasts were found to be skilful for all times of day and lead times considered. Thus, with an appropriate probability threshold applied, the nowcasts are useful at predicting both convective activity over the Western Sahelian domain, and extreme precipitation events over Dakar. Assessing the skill of the probability *values* according to BSS shows skill varying with the time of day, peaking in the afternoon where the probability values are skilful out to five hours, with a minimum in skill in the evening where skill is seen in the first three hours. The applicability of these results to other regions across Africa is currently being tested, where we expect the largest potential for locations that are similarly dominated by long-lived, propagating convective systems. Although a direct like-for-like comparison with existing approaches for nowcasting future tracks of convection as in Burton *et al.* (2022) and Hill *et al.* (2020) is not possible (e.g., due to differences in reference, domain, verification data), they do provide a useful context in which to consider the probabilistic approach presented here. Burton *et al.* (2022) produce nowcasts skilful out to four hours, with minimum skill in the afternoon. Hill *et al.* (2020) show nowcasts are skilful out to the 90 minutes considered, but do not assess longer lead times. The climatology-based probabilistic nowcasts presented here also show skill out to the six hour lead times considered, with skill peaking in the afternoon. Combined with the very limited data used (MSG CTT only) and minimal calculations required in NRT, this suggests the probabilistic nowcasts could be highly valuable for operational use in the near-term, particularly in the afternoon and early evening when convective activity and nowcast skill peak. As this time of day corresponds to the minimum skill found for track-based nowcasting (Burton *et al.*, 2022) these approaches, whilst being very different, may be particularly complementary; combining these in a real-time operational system would provide a more complete picture of impeding hazards from severe convection which should be investigated in future work.

The method presented in this paper has made use of a neighbourhood approach to define probabilities at different spatial scales. This has been implemented in two

places, first in defining the source area S_0 — the distance around current convective structures used to condition the historical data — and secondly in defining the scales L over which the probabilities are calculated. Whereas S_0 was fixed based on the size of the historical sample needed to give spatially consistent probability values at a useful granularity, a range of L were considered with forecast performance used to inform the final selection for NRT use. This final selection, obtained quantitatively from manually looking at all the verification data, varied with forecast lead time, ranges from 45 km at the nowcast origin to 105 km at lead times of six hours. At short lead times, these scales are comparable to those found to be skilful for the verification of track-based nowcasts by Burton *et al.* (2022): 10 km at two hours. However, differences are seen at longer lead times, with Burton *et al.* (2022) suggesting 200 km as skilful at four hours, compared to the 85 km L selected here at this lead time. Although differently defined, Burton *et al.* (2022) make use of the useful scales defined by the Fractions Skill Score (Roberts & Lean, 2008). This comparison does suggest that the climatological probabilities are retaining smaller-scale information at longer lead times. This makes sense as the diurnal cycle of convection, and fixed surface constraints on convection initiation and decay, are implicitly included in the climatological information. In contrast, the object tracking method of Burton *et al.* (2022) takes no account of the convective life cycle, and how it is strongly influenced by both the diurnal cycle and underlying terrain.

The methods discussed above are only a selection of those available to use for observation-based nowcasting. In particular, current research into machine learning is providing exciting opportunities for the development of novel nowcasting techniques (Kumar *et al.*, 2020; Shi *et al.*, 2017). There are also similarities between the conditional probabilistic approach presented here, to that of *analogue forecasting* where the historical database is searched to find the past events most like the current meteorological situation (e.g., Foresti *et al.*, 2015; Panziera *et al.*, 2011). However, our approach differs in that there is no matching to single historical events; probabilistic nowcasts are generated from multiple storms sourced in similar locations to that which is observed. Secondly, probabilities are created separately for each current convective structure and combined: the full pattern of observed convection in the real-time image is not matched to that from the historical database, as this would result in a small unrepresentative sample. Based fully on historical observations (here from 2004 to 2019), the simple nowcasting method presented here will only forecast convective activity at locations where convection occurred in the historical sample. If rainfall patterns were to change to different locations, these would not be captured. It would however be possible to periodically update the climatological probabilities $P(C)$ and $P(C_t|\boldsymbol{x}_0)$.

Although this study calculated and initiated nowcasts hourly, as a simple proof-of-concept, it is possible for nowcasts to be calculated and initiated up to the 15-min temporal resolution of the MSG CTT data. For fast-developing systems close to specific areas of interest, for example settlements, this could provide more timely information. However, the gains in skill from any increase in temporal granulation would have to be carefully considered, given the inherent link between spatial uncertainty and temporal uncertainty for forward-propagating systems. Here we do not separately consider temporal uncertainty. Given calibrated skill (as given by the ROCSS) was seen out to the maximum lead time of six hours considered here, it is possible that additional information could be gained by further extending the nowcasts, given MCS lifetime in this region can extend to up to 24 hours. Of course, these extended forecasts would require further in-depth analysis to understand the underlying drivers of predictability, and cautious interpretation.

This paper has focused on the development of gridded nowcasts of convective structures, applicable across a wide geographical region. Ongoing work seeks to relate these probabilities of convection more directly to extreme precipitation risk, and to quantify the associated hazard of flash flooding. The system could be further improved by including additional meteorological information, either observed or forecast. For example, as land surface temperature (LST) has been shown to constrain the development of convection (Klein & Taylor, 2020; Taylor *et al.*, 2022), including LST in the nowcasting system could lead to improvements in skill. Including further convective structure properties, such as temperature or size, and larger-scale atmospheric information related to convective initiation, could also lead to improvements. Further refinements and constraints to the historical sample could also be considered, such as introducing monthly variation to the conditional probabilities.

6 | CONCLUSIONS

In conclusion, a simple probabilistic nowcasting methodology has been presented and verified for predicting convective structures over the Western Sahel. Based on one stream of satellite data, MSG CTT, and using minimal real-time computational resource (nowcasts can be produced in around 5 min on a standard laptop), this provides a useful and easily-implemented method widely

applicable across data scarce regions with limited radar coverage. Nowcasts are based on prior offline database calculations which, although non-complex, are computationally intense (requiring the use of high performance computing platforms).

Through verifying the nowcast performance against both observed convective structures, and 24-hour rain gauge accumulation data over Dakar, it has been shown that these nowcasts are skilful out to six hour lead times compared to the full climatology. We also showed that suitable spatial scales for calculating the probabilities vary with lead time from 45 km at the nowcast origin to around 100 km at a six hour lead time.

These methods provide a baseline and a framework from which more sophisticated nowcasts can be produced and assessed, for example including additional meteorological variables or combining with other nowcasting approaches, such as the prediction of storm tracks. Additionally, when linked with the chance of extreme precipitation, the probabilistic nowcasts can be used to estimate extreme precipitation and associated flooding hazards.

ACKNOWLEDGEMENTS

EUMETSAT are gratefully acknowledged for providing the satellite data. We thank the two anonymous reviewers for their comments which substantially improved this study. This work benefited enormously from discussions with colleagues, in particular Steven Wells at UKCEH, and workshops with forecasters at ANACIM whose local expertise and rain gauge observation data over Dakar were vital in developing and verifying the nowcasting methods.

FUNDING INFORMATION

This work was supported by the Natural Environment Research Council (NERC) and Foreign, Commonwealth and Development Office (FCDO) Science for Humanitarian Emergencies and Resilience (SHEAR) programme through the Nowcasting Flood Impacts of Convective Storms in the Sahel (NFLICS) project (grant number NE/S006087/2), the UK Research and Innovation (UKRI) Global Challenges Research Fund, African Science for Weather Information and Forecasting Techniques (SWIFT) programme (grant number NE/P021077/1), and the NERC NC-International programme (grant number NE/X006247/1) delivering National Capability.

DATA AVAILABILITY STATEMENT

The Meteosat Second Generation (MSG) data that support the findings of this study are openly available at the EUMETSAT website https://www.eumetsat.int/, MSG channel 9 10.8μm. The algorithm for identification of convective activity is openly available on github: https://github.com/cornkle/ccores

ORCID

Seonaid R. Anderson https://orcid.org/0000-0001-8556-577X
Steven J. Cole https://orcid.org/0000-0003-4294-8687
Cornelia Klein https://orcid.org/0000-0001-6686-0458
Christopher M. Taylor https://orcid.org/0000-0002-0120-3198
Cheikh Abdoulahat Diop https://orcid.org/0000-0002-8457-6175

REFERENCES

Brier, G. (1950) Verification of forecasts expressed in terms of probability. *Monthly Weather Review*, 78(1), 1–3. Available from: https://doi.org/10.1175/1520-0493(1950)078%3C0001:VOFEIT%3E2.0.CO;2

Browning, K.A. (1982) *Nowcasting*. London: Academic.

Buizza, R. (1997) Potential forecast skill of ensemble prediction and spread and skill distributions of the ECMWF ensemble prediction system. *Monthly Weather Review*, 125(1), 99–119. Available from: https://doi.org/10.1175/1520-0493(1997)125<0099:PFSOEP>2.0.CO;2

Burton, R.R., Blyth, A.M., Groves, J., Lamptey, B.L., Fletcher, J.K., Marsham, J.H. et al. (2022) Satellite-based Nowcasting of west African mesoscale storms has skill at up to 4-h Lead time. *Weather and Forecasting*, 37, 445–455. Available from: https://doi.org/10.1175/WAF-D-21-0051.1

Dey, S.R.A., Leoncini, G., Roberts, N.M., Plant, R.S. & Migliorini, S. (2014) A spatial view of ensemble spread in convection permitting ensembles. *Monthly Weather Review*, 142(11), 4091–4107. Available from: https://doi.org/10.1175/MWR-D-14-00172.1

Dey, S.R.A., Roberts, N.M., Plant, R.S. & Migliorini, S. (2016) A new method for the characterization and verification of local spatial predictability for convective-scale ensembles. *Quarterly Journal of the Royal Meteorological Society*, 142(698), 1982–1996. Available from: https://doi.org/10.1002/qj.2792

Di Baldassarre, G., Montanari, A., Lins, H., Koutsoyiannis, D., Brandimarte, L. & Blschl, G. (2010) Flood fatalities in Africa: from diagnosis to mitigation. *Geophysical Research Letters*, 37(22), 2–6. Available from: https://doi.org/10.1029/2010GL045467

Ebert, E.E. (2008) Fuzzy verification of high-resolution gridded forecasts: a review and proposed framework. *Meteorological Applications*, 15, 51–64. Available from: https://doi.org/10.1002/met.25

Engel, T., Fink, A.H., Knippertz, P., Pante, G. & Bliefernicht, J. (2017) Extreme precipitation in the west African cities of Dakar and Ouagadougou: atmospheric dynamics and implications for flood risk assessments. *Journal of Hydrometeorology*, 18(11), 2937–2957. Available from: https://doi.org/10.1175/JHM-D-16-0218.1

EUMETSAT. (2022a) European organisation for the exploitation of meteorological satellites. https://www.eumetsat.int/

EUMETSAT. (2022b) EUMETSAT earth observation portal. https://eoportal.eumetsat.int/cas/login

Foresti, L., Panziera, L., Mandapaka, P.V., Germann, U. & Seed, A. (2015) Retrieval of analogue radar images for ensemble nowcasting of orographic rainfall. *Meteorological Applications*, 155(2013), 141–155. Available from: https://doi.org/10.1002/met.1416

Futyan, J.M. & Del Genio, A.D. (2007) Deep convetive system evolution over Africa and the tropical Atlantic. *Journal of Climate*, 20(20), 5041–5060. Available from: https://doi.org/10.1175/JCLI4297.1

Gilleland, E., Ahijevych, D., Brown, B.G., Casati, B. & Ebert, E.E. (2009) Intercomparison of spatial forecast verification methods. *Weather and Forecasting*, 24(5), 1416–1430. Available from: https://doi.org/10.1175/2009WAF2222269.1

Guy, N. & Rutledge, S.A. (2012) Regional comparison of west African convective characteristics: a TRMM-based climatology. *Quarterly Journal of the Royal Meteorological Society*, 138(666), 1179–1195. Available from: https://doi.org/10.1002/qj.1865

Hill, P.G., Stein, T.H.M., Roberts, A.J., Fletcher, J.K., Marsham, J.H. & Groves, J. (2020) How skilful are Nowcasting Satellite Applications Facility products for tropical Africa? *Meteorological Applications*, 27(6), 1–14, Available from: https://doi.org/10.1002/met.1966

Hohenegger, C. & Schär, C. (2007) Predictability and error growth dynamics in cloud-resolving models. *Journal of the Atmospheric Sciences*, 64(12), 4467–4478. Available from: https://doi.org/10.1175/2007JAS2143.1

Jolliffe, I.T. & Stephenson, D.B. (2012) *Forecast verification: a practitioner's guide in atmospheric science* (2nd ed.). John Wiley & Sons Ltd. 274 pp.

Keat, W.J., Stein, T.H.M., Phaduli, E., Landman, S., Becker, E., Bopape, M.J.M. et al. (2019) Convective initiation and storm life cycles in convection-permitting simulations of the met Office unified model over South Africa. *Quarterly Journal of the Royal Meteorological Society, October*, 2018, 1323–1336. Available from: https://doi.org/10.1002/qj.3487

Klein, C., Belušić, D. & Taylor, C.M. (2018) Wavelet scale analysis of mesoscale convective systems for detecting deep convection from infrared imagery. *Journal of Geophysical Research: Atmospheres*, 123(6), 3035–3050. Available from: https://doi.org/10.1002/2017JD027432

Klein, C. & Taylor, C.M. (2020) Dry soils can intensify mesoscale convective systems. *PNAS*, 117(35), 21132–21137. Available from: https://doi.org/10.1073/pnas.2007998117

Kniffka, A., Knippertz, P., Fink, A.H., Peter, B., Marlon, G.H., Pante, G. et al. (2020) An evaluation of operational and research weather forecasts for southern West Africa using observations from the DACCIWA field campaign in June – July 2016. https://doi.org/10.1002/qj.3729

Kumar, A., Islam, T., Sekimoto, Y., Mattmann, C. & Wilson, B. (2020) Convcast: an embedded convolutional LSTM based architecture for precipitation nowcasting using satellite data. *PLoS One*, 15(3), 1–18. Available from: https://doi.org/10.1371/journal.pone.0230114

Leutbecher, M. & Palmer, T.N. (2008) Ensemble forecasting. *Journal of Computational Physics*, 227(7), 3515–3539. Available from: https://doi.org/10.1016/j.jcp.2007.02.014

Maidment, R.I., David, G., Elena, T., Marc, S., Tim, H., Rob, R. et al. (2014) The 30 year TAMSAT African rainfall climatology and time series (TARCAT) data set. *Journal of Geophysical Research: Atmospheres*, 119(18), 10619–10644. https://doi.org/10.1002/2014JD021927

Maranan, M., Fink, A.H. & Knippertz, P. (2018) Rainfall types over southern West Africa: objective identification, climatology and synoptic environment. *Quarterly Journal of the Royal Meteorological Society*, 144, 1628–1648. Available from: https://doi.org/10.1002/qj.3345

Mathon, V., Laurent, H. & Lebel, T. (2002) Mesoscale convective system rainfall in the Sahel. *Journal of Applied Meteorology*, 41(11), 1081–1092. Available from: https://doi.org/10.1175/1520-0450(2002)041<1081:MCSRIT>2.0.CO;2

Melhauser, C. & Zhang, F. (2012) Practical and intrinsic predictability of severe and convective weather at the mesoscales. *Journal of the Atmospheric Sciences*, 69(11), 3350–3371. Available from: https://doi.org/10.1175/JAS-D-11-0315.1

Nesbitt, S.W., Cifelli, R. & Rutledge, S.A. (2006) Storm morphology and rainfall characteristics of TRMM precipitation features. *Monthly Weather Review*, 134(10), 2702–2721. Available from: https://doi.org/10.1175/MWR3200.1

NWCSAF. (2022) Nowcasting satellite applications facility. https://www.nwcsaf.org/

Panthou, G., Lebel, T., Vischel, T., Quantin, G., Sane, Y., Ba, A. et al. (2018) Rainfall intensification in tropical semi-arid regions: the Sahelian case. *Environmental Research Letters*, 13(6), 064013. Available from: https://doi.org/10.1088/1748-9326/aac334

Panziera, L., Germann, U., Gabella, M. & Mandapaka, P.V. (2011) NORA – Nowcasting of orographic rainfall by means of analogues. *Quarterly Journal of the Royal Meteorological Society*, 137, 2106–2123. Available from: https://doi.org/10.1002/qj.878

Prein, A.F., Rasmussen, R.M., Wang, D. & Giangrande, S.E. (2021) Sensitivity of organized convective storms to model grid spacing in current and future climates. *Philosophical Transactions of the Royal Society*, *379*(2195), 20190546. Available from: https://doi.org/10.1098/rsta.2019.0546

Pulkkinen, S., Nerini, D., Pérez Hortal, A.A., Velasco-Forero, C., Seed, A., Germann, U. et al. (2019) Pysteps: an open-source python library for probabilistic precipitation nowcasting (v1.0). *Geoscientific Model Development*, 12(10), 4185–4219. Available from: https://doi.org/10.5194/gmd-12-4185-2019

Reinares Martínez, I. & Chaboureau, J.-P. (2018) Precipitation and mesoscale convective systems: explicit versus parameterized convection over northern Africa. *Monthly Weather Review*, 146, 812. Available from: https://doi.org/10.1175/MWR-D-17-0202.1

Roberts, A.J., Fletcher, J.K., Groves, J., Marsham, J.H., Parker, D.J., Blyth, A.M. et al. (2021) Nowcasting for Africa: advances, potential and value. *Weather*, 77(7), 250–256. Available from: https://doi.org/10.1002/wea.3936

Roberts, N.M. & Lean, H.W. (2008) Scale-selective verification of rainfall accumulations from high-resolution forecasts of convective events. *Monthly Weather Review*, 136(1), 78–97. Available from: https://doi.org/10.1175/2007MWR2123.1

Roca, R. & Fiolleau, T. (2020) Extreme precipitation in the tropics is closely associated with long-lived convective systems. *Communications Earth & Environment*, 1(1), 1–6. Available from: https://doi.org/10.1038/s43247-020-00015-4

Schwartz, C.S. & Sobash, R.A. (2017) Generating probabilistic forecasts from convection-allowing ensembles using neighborhood approaches: a review and recommendations. *Monthly Weather Review*, 145, 3397–3418. Available from: https://doi.org/10.1175/MWR-D-16-0400.1

Shi, X., Gao, Z., Lausen, L., Wang, H., Yeung, D.Y., Wong, W.K. et al. (2017) Deep learning for precipitation nowcasting: a benchmark and a new model. *Advances in Neural Information Processing Systems*, 30. https://proceedings.neurips.cc/paper_files/paper/2017/file/a6db4ed04f1621a119799fd3d7545d3d-Paper.pdf

Taylor, C.M., Belusic, D., Guichard, F., Parker, D.J., Vischel, T., Bock, O. et al. (2017) Frequency of extreme Sahelian storms tripled since 1982 in satellite observations. *Nature*, 544(7651), 475–478. Available from: https://doi.org/10.1038/nature22069

Taylor, C.M., Klein, C., Dione, C., Parker, D.J., Marsham, J., Abdoulahat Diop, C. et al. (2022) Nowcasting tracks of severe convective storms in West Africa from observations of land surface state. *Environmental Research Letters*, 17(3), 034016. Available from: https://doi.org/10.1088/1748-9326/ac536d

Tramblay, Y., Villarini, G. & Zhang, W. (2020) Observed changes in flood hazard in Africa. *Environmental Research Letters*, 15(10), 1040b5. Available from: https://doi.org/10.1088/1748-9326/abb90b

UKCEH. (2023) Hydrology in Sub-Saharan Africa portal. https://eip.ceh.ac.uk/hydrology/west-africa/nowcasting/

UKRI. (2022) NEC06809 NFLICS: Nowcasting flood impacts of convective storms in the sahel. https://gtr.ukri.org/projects?ref=NE%2FS006087%2F2

Vogel, P., Knippertz, P., Fink, A.H., Schlueter, A. & Gneiting, T. (2018) Skill of global raw and postprocessed ensemble predictions of rainfall over northern tropical Africa. *Weather and Forecasting*, 33(2), 369–388. Available from: https://doi.org/10.1175/WAF-D-17-0127.1

Wilks, D.S. (2011) *Statistical Methods in the atmospheric sciences (3rd ed)*. Academic Press. 704 pp.

ZAMG. (2017) Algorithm theoretical basis document for the extrapolated imagery processor of the NWC/GEO. Online http://www.nwcsaf.org/AemetWebContents/ScientificDocumentation/Documentation/GEO/v2016/NWC-CDOP2-GEO-ZAMG-SCI-ATBD-EXIM_v1.1.pdf

SUPPORTING INFORMATION

Additional supporting information can be found online in the Supporting Information section at the end of this article.

How to cite this article: Anderson, S.R., Cole, S.J., Klein, C., Taylor, C.M., Diop, C.A. & Kamara, M. (2024) Nowcasting convective activity for the Sahel: A simple probabilistic approach using real-time and historical satellite data on cloud-top temperature. *Quarterly Journal of the Royal Meteorological Society*, 1–21. Available from: https://doi.org/10.1002/qj.4607